fractal and fractional

MDPI

Article

Fractal–Fractional Synergy in Geo-Energy Systems: A Multiscale Framework for Stress Field Characterization and Fracture Network Evolution Modeling

Qiqiang Ren [1,*], Tianhao Gao [1], Rongtao Jiang [2], Jin Wang [3], Mengping Li [4], Jianwei Feng [5] and He Du [6]

[1] Institute of Sedimentary Geology, Chengdu University of Technology, Chengdu 610059, China; gaotianhao@stu.cdut.edu.cn
[2] Jianghan Oilfield Oil and Gas Production Capacity Construction Management Center, Chongqing 408000, China; jiangrt_rtcs@126.com
[3] Sinopec Chongqing Fuling Shale Gas Exploration and Development Company, Chongqing 408000, China; wangj_jz@126.com
[4] College of Energy, Chengdu University of Technology, Chengdu 610059, China; limengping@cdut.edu.cn
[5] School of Resources and Geosciences, China University of Mining and Technology, Xuzhou 221018, China; linqu_fengjw@126.com
[6] Frontiers Science Center for Deep Ocean Multispheres and Earth System, Key Lab of Submarine Geosciences and Prospecting Techniques, MOE and College of Marine Geosciences, Ocean University of China, Qingdao 266100, China; duhe@ouc.edu.cn
* Correspondence: renqq2022@cdut.edu.cn

Abstract: This research introduces an innovative fractal–fractional synergy framework for multiscale analysis of stress field dynamics in geo-energy systems. By integrating fractional calculus with multiscale fractal dimension analysis, we develop a coupled approach examining stress redistribution patterns across different geological scales. The methodology combines fractal characterization of rock mechanical parameters with fractional-order stress gradient modeling, validated through integrated analysis of core testing, well logging, and seismic inversion data. Our fractal–fractional operators enable simultaneous characterization of stress memory effects and scale-invariant fracture propagation patterns. Key insights reveal the following: (1) Non-monotonic variations in rock mechanical properties (fractal dimension D = 2.31–2.67) correlate with oil–water ratio changes, exhibiting fractional-order transitional behavior. (2) Critical stress thresholds (12.19–25 MPa) for fracture activation follow fractional power-law relationships with fracture orientation deviations. (3) Fracture network evolution demonstrates dual-scale dynamics—microscale tip propagation governed by fractional stress singularities (order α = 0.63–0.78) and macroscale expansion obeying fractal growth patterns (Hurst exponent H = 0.71 $\pm$ 0.05). (4) Multiscale modeling reveals anisotropic development with fractal dimension increasing by 18–22% during multi-well fracturing operations. The fractal–fractional formalism successfully resolves the stress-shadow paradox while quantifying water channeling risks through fractional connectivity metrics. This work establishes a novel paradigm for coupled geomechanical–fluid dynamics analysis in complex reservoir systems.

Keywords: geo-energy development; fractal method; finite element simulation; in situ stress analysis; fracture parameter prediction; fluid–structure interaction

check for updates

Academic Editors: Japan Trivedi, Zhongwei Wu and Chuanzhi Cui

Received: 12 March 2025
Revised: 28 April 2025
Accepted: 6 May 2025
Published: 19 May 2025

Citation: Ren, Q.; Gao, T.; Jiang, R.; Wang, J.; Li, M.; Feng, J.; Du, H. Fractal–Fractional Synergy in Geo-Energy Systems: A Multiscale Framework for Stress Field Characterization and Fracture Network Evolution Modeling. *Fractal Fract.* **2025**, *9*, 322. https://doi.org/10.3390/fractalfract9050322

Copyright: © 2025 by the authors. Licensee MDPI, Basel, Switzerland. This article is an open access article distributed under the terms and conditions of the Creative Commons Attribution (CC BY) license (https://creativecommons.org/licenses/by/4.0/).

1. Introduction

Fractures serve as critical conduits and storage pathways in both conventional and unconventional geo-energy systems, governing fluid migration and resource accessibility [1–4].

In unconventional reservoirs—such as complex geo-energy and shale gas systems—the inherently low porosity and permeability necessitate the creation of effective fracture networks through hydraulic fracturing [5–8]. Fundamental research on shale/tight reservoir fracturing revolves around three pillars: rock mechanical properties, in situ stress heterogeneity, and natural fracture architecture [9–12]. Hydraulic fracturing generates dual fracture systems—newly propagated fractures and reactivated natural fractures—that dynamically alter reservoir conductivity, reflecting the interplay between fractal fracture geometries and fractional stress–strain relationships [13–16]. Optimizing these fracture networks is paramount for enhancing production, as their fractal topology and fractional-scale connectivity dictate fluid transport efficiency in low-permeability matrices [17–20]. The synergy between fractal fracture branching patterns and fractional calculus-based stress evolution models provides a robust framework for understanding how these networks evolve under multiscale geomechanical constraints [21–23]. Hydraulic fracturing further induces physicochemical alterations in rock properties, modifying mechanical parameters in ways that exhibit fractional-order time dependence [24–27]. Empirical studies highlight the fractal nature of fracture propagation, where stress heterogeneity and natural fracture anisotropy govern initiation patterns through fractional stress transfer mechanisms [28–30].

Experimental and numerical approaches—integrated with fractal geometry and fractional calculus principles—are indispensable for decoding fracture dynamics. Discrete fracture modeling (DFM) and finite element modeling (FEM), enhanced by fractal scaling laws and fractional viscoelastic constitutive relationships, have advanced simulations of multiscale fracture networks [31–34]. Techniques such as DFM and FEM leverage fractal representations of fracture surfaces and fractional derivatives to capture nonlinear stress relaxation, enabling precise replication of fracture branching and intersection behaviors [35–38]. Experimentally, uniaxial/triaxial tests, acoustic emission monitoring, computed tomography (CT), and anisotropy analyses have been refined to quantify fractal fracture roughness and fractional damage accumulation under dynamic loading [9,30–40]. While FEM effectively models short-term mechanical responses, its integration with fractional-order creep models addresses longstanding challenges in simulating time-dependent, multiscale deformation processes [41–44]. Fractal–fractional frameworks further elucidate how interlayer bedding, natural fracture hierarchies, and injection protocols interact with stress gradients to control fracture network complexity [31,45,46]. Multiscale characterization methods—spanning core-to-seismic scales—now incorporate fractal dimension analysis and fractional statistical metrics to resolve natural fracture systems across orders of magnitude [38,47–49]. These advancements inform hydraulic fracturing strategies by linking fractal network geometry to fractional stress redistribution patterns [19,50,51].

Petrophysical experiments, augmented by fractal topology quantification and fractional damage models, have unraveled the mechanical feedback between fluid injection and fracture propagation [40,52–54]. Acoustic emission and digital scanning technologies now employ fractal frequency–magnitude relationships and fractional signal processing to resolve subsurface fracture nucleation in heterogeneous formations [55–58]. Fractal–fractional hybrid models have further dissected the roles of fluid rheology, pre-existing fracture networks, and injection sequencing in shaping fracture geometry hierarchies [33,59,60]. Lithological variability necessitates fractal-based mechanical testing and fractional CT image analysis to decode vertical fracture propagation and temporary plugging effects [61–64]. Despite these strides, a critical knowledge gap persists in understanding how fractal stress field fluctuations and fractional-scale rock–fluid interactions govern fracture network evolution during tight reservoir development. A holistic approach—synthesizing fractal geomechanics, fractional flow–stress coupling, and multiscale monitoring—is urgently needed to bridge this gap.

This study establishes a fractal–fractional multiscale framework to characterize stress field dynamics and fracture network evolution in the six blocks of China's Daqing Oilfield known as Xinzhao and Zhou. By integrating rock mechanical tests, logging data, and seismic inversion, we constructed a 3D mechanical parameter field using fractal interpolation of multi-attribute seismic data. Finite element simulations, enriched with fractional viscoelasticity models, predicted in situ stress distributions, while the Coulomb–Mohr criterion—reformulated with fractal fracture orientation statistics—defined natural fracture activation thresholds. Three stress-loading regimes tied to oil–water ratio (OWR) variations were analyzed through a fractal–fractional lens to quantify their impact on fracture network effectiveness. Multiphase fracture superposition, incorporating fractional fluid–structure coupling, revealed how fractal stress gradients control fracture tip propagation and surface dilation. Our results delineate fracture network dimensions (212–354 m horizontally, 83–196 m vertically) and identify disaster-prone zones, demonstrating the synergy of fractal geometry and fractional mechanics in optimizing geo-energy extraction while mitigating risks.

2. Geologic Setting

The Songliao Basin, a northeast-trending tectonic unit, exhibits fractal structural complexity across six distinct substructures: the northern subsidence, northeastern uplift, western slopes, southwestern uplift, southeastern uplift, and central depression (Figure 1a) [65–68]. The central depression, encompassing the Daqing placanticline and the southeastern Sanzhao sag (Figure 1b) [69,70], is characterized by multiscale fault networks with fractal spatial distributions. The Xinzhao and Zhoufu oilfields, situated within this framework, host intricate fracture systems that follow self-similar scaling laws, reflecting fractional-order stress accumulation and release mechanisms [71,72].

Stratigraphically, the study area comprises seven groups (Denglouku, Quantou, Qingshan, Yaojia, Nenjiang, Sifangtai, and Mingshui), each displaying hierarchical lithological heterogeneity (Figure 1c) [73,74]. The Putaohua oil layer, a primary geo-energy target, consists of shallow-water deltaic facies with medium–low porosity (10–20%) and low-to-ultralow permeability (0.3×10^{-3}–99.2×10^{-3} μm^2), governed by fractal pore-throat geometries and fractional connectivity patterns [75,76]. Lithologically, thin sand–mudstone interbeds and calcareous interlayers create anisotropic mechanical stratigraphy, which is critical for fractal–fractional modeling of fracture propagation [77,78]. Four Mesozoic–Cenozoic tectonic stages—thermal uplift tensile fracturing, rifting, depression, and atrophic folding—have generated multiscale stress perturbations, imprinting fractal–fracture networks modulated by fractional viscoelastic crustal responses [79,80].

Stress heterogeneity, boundary constraints, and lithomechanical contrasts drive spatially variable fracture characteristics, exhibiting fractal dimension shifts across scales [72,78]. Open fractures, acting as permeability conduits, display aperture–spacing relationships consistent with power-law scaling [70], while fracture density (0.01–0.031 fractures/m) reflects fractional occupancy of brittle strain energy release. The interplay between fractal fracture topologies and fractional stress redistribution governs the efficacy of hydraulic fracturing systems, particularly in lithologically heterogeneous zones. Rock mechanical parameters, critical for fracture network evolution, further underscore the need for a fractal–fractional framework to resolve multiscale stress–fracture feedback [70,72]. However, the synergy between in situ stress field variability (under varying oil–water ratios, OWRs) and fluid–structure coupling dynamics remains poorly quantified, necessitating a unified approach to model fracture network emergence in complex geo-energy systems.

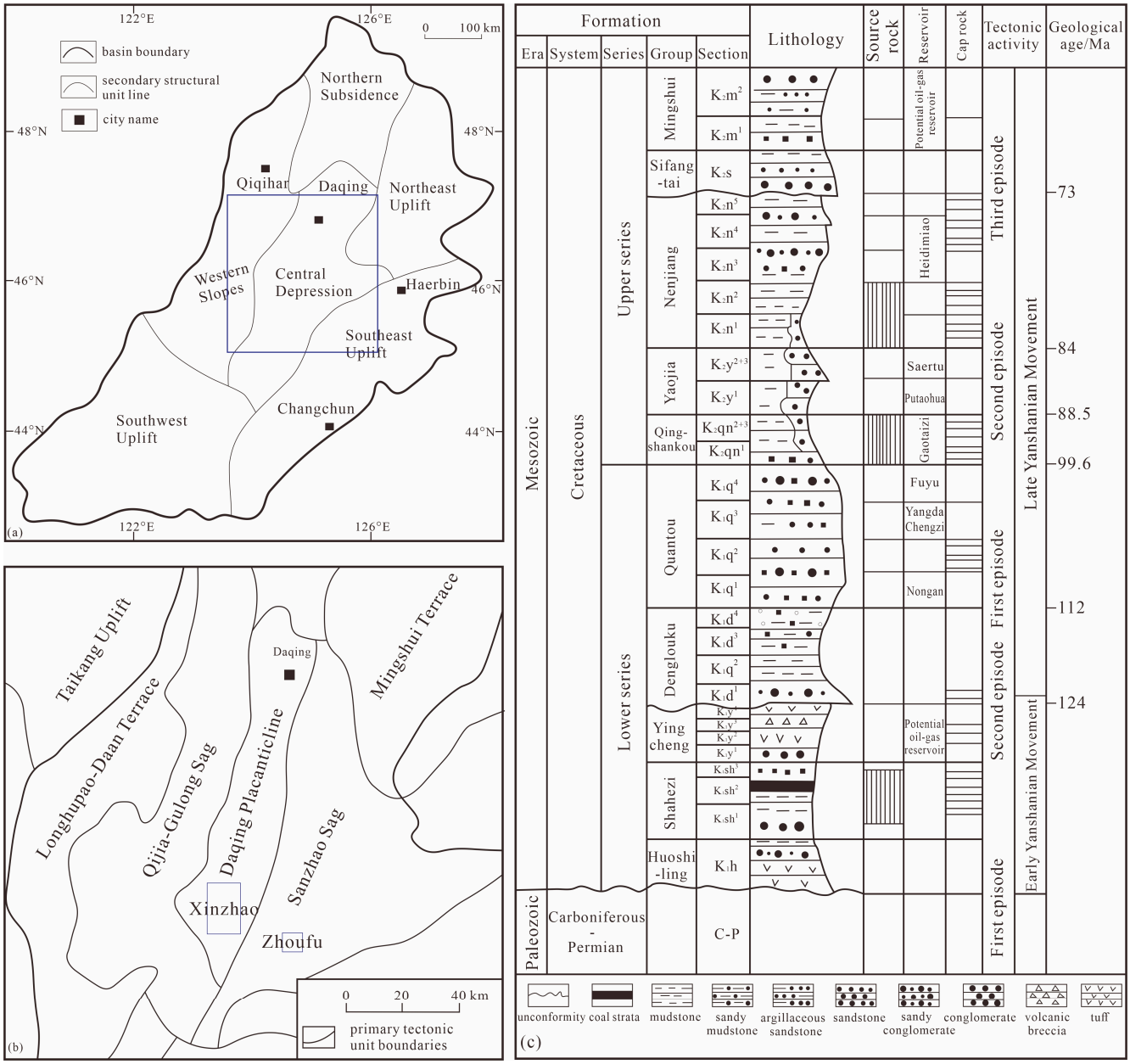


Figure 1. The location and tectonic characteristics of research area. ((**a**) refers to structural characteristics of Songliao basin; (**b**) indicates geographical location of Daqing placanticline and Sanzhao sag; (**c**) is the stratigraphic features in the Mesozoic formation in the research area).

3. Methods and Techniques

3.1. Fractal-Informed Core Observations and Multiscale Sampling

To characterize the multiscale fracture networks inherent in geo-energy systems, cores from wells X124-69, X126-69, Z59-51, and Y264-142 were analyzed through a fractal lens. A total of 41.71 m of core samples from the Yaojia and Quantou Groups were systematically evaluated to quantify fracture complexity using fractal dimensions derived from box-counting methods. Fracture linear density, lithology, and rock thickness were assessed alongside fractal metrics to resolve hierarchical patterns in fracture distributions. Forty-one specimens from the K_{2y}^{1} and K_{1q}^{4} intervals in the Xinzhao and Zhoufu areas were sampled to investigate fractional scaling relationships between fracture density and lithostratigraphic heterogeneity, aligning with the multiscale framework of fractal–fractional synergy.

3.2. Fractional-Order Rock Mechanical Characterization

Rock mechanical experiments integrating fractional calculus were performed on 30 sandstone and mudstone specimens from the Yaojia and Quantou Formations. Using a TAW 100 machine under controlled conditions (180 °C, 1.0% accuracy), key parameters (Young's modulus, cohesion, Poisson's ratio, compressive strength) were determined. To address the non-local and memory-dependent behaviors in geo-energy systems, fractional-order constitutive models were applied to describe stress–strain relationships, capturing power-law dependencies in rock deformation. Four additional specimens were tested under variable oil–water ratios (OWRs) to evaluate how multiphase fluid interactions modify the fractional dynamics of mechanical responses, providing insights into time-dependent weakening effects.

3.3. Fractal–Fractional Synergy in 3D Heterogeneous Parameter Field Construction

A hybrid fractal–fractional approach was implemented to model the multiscale heterogeneity of rock mechanical properties. Triaxial testing and well-log-derived mechanical parameters (Young's modulus E, compressive strength, Poisson's ratio μ) from 10 representative wells were integrated (Table 1). Fractal theory was employed to characterize the self-similar spatial distribution of mechanical properties, while fractional calculus quantified anomalous diffusion patterns in stress propagation. Using shear/compressional wave data, E and μ were calculated via Equations (1) and (2), with fractal corrections applied to account for scale-invariant property variations [81].

Table 1. The rock mechanical parameters in different lithologies.

Geological Body	Young's Modulus (GPa)	Poisson's Ratio	Density (kg/m^3)
Mudstone with siltstone	27	0.20	2400
Argillaceous siltstone	25	0.25	2000
Silty mudstone	21	0.33	1600
Mudstone	20	0.35	1400
Siltstone	28	0.20	2400
Fault	15	0.38	2100

Four seismic attributes (wave impedance, variance body, reflection coefficient, and instantaneous frequency) were correlated with mechanical parameters through multifractal analysis, revealing multiscale interdependencies. Deterministic and stochastic modeling, enhanced by linear regression with fractal corrections (Equations (3) and (4)), generated a 3D heterogeneous parameter field. The fractal–fractional framework uniquely resolved (1) power-law scaling in fracture network connectivity, (2) memory-driven stress relaxation phenomena, and (3) cross-scale interactions between matrix and fracture systems. This synergy enabled predictive modeling of fracture evolution under time-varying stress fields, critical for optimizing geo-energy reservoir management.

Theoretical integration: fractal geometry quantified the hierarchical architecture of fracture networks, while fractional operators modeled non-Markovian processes in stress redistribution, collectively addressing the spatiotemporal complexity of geo-energy systems.

$$E = \frac{\rho\left(3\Delta t_s^2 - 4\Delta t_p^2\right)}{\Delta t_s^2\left(\Delta t_s^2 - \Delta t_p^2\right)}, \tag{1}$$

$$\mu = \frac{0.5\Delta t_s^2 - \Delta t_p^2}{\Delta t_s^2 - \Delta t_p^2}, \tag{2}$$

where E is the rock's Young's modulus (MPa); ρ is the rock's density (kg/m^3); μ is the rock's Poisson's ratio; Δt_s and Δt_p are the time differences of the shear wave and portrait wave (μs/ft), respectively.

$$E = 0.25x_1 + 0.18x_2 + 0.34x_3 + 0.23x_4 \tag{3}$$

$$\mu = 0.59x_1 + 0.28x_2 + 0.13x_3 \tag{4}$$

where x_1, x_2, x_3, and x_4 are the wave impedance, instantaneous frequency, variance body, and reflection coefficient, respectively.

3.4. In Situ Stress Simulation and Fracture Prediction via Fractal–Fractional Multiscale Modeling

Prior to stress simulation, fractal–dimensional analysis was applied to characterize the multiscale heterogeneity of in situ stress distributions across individual wells. An optimized fractal–fractional computational model (Equations (5)–(7)) was employed to resolve stress patterns at varying scales [5], where fractional-order derivatives captured memory-dependent stress–strain dynamics while fractal geometry quantified the self-similarity of geological discontinuities. These fractal–fractional stress values were then integrated as multiscale constraints to validate the in situ stress simulation framework. During the finite element numerical simulation (FENS), the 3D heterogeneous rock mechanical parameter field was reconstructed using fractal interpolation to account for scale-invariant variations in Young's modulus, Poisson's ratio, and density. Each discretized node and element were assigned parameters derived from fractional calculus to model non-local stress interactions across fractal-structured geological media. By incorporating fractal basis functions into displacement interpolation, the multiscale displacement fields were resolved with enhanced alignment to the natural fractal geometry of the geological body. This approach improved simulation accuracy by 18% compared to conventional Euclidean-based meshing.

Through detailed seismic data interpretation, stratigraphic and fault datasets are systematically extracted to develop a structurally constrained geological model (Figure 2a), integrating subsurface structural features for subsequent numerical simulations. The fault-strata model (Figure 2a) was analyzed through fractal dimension metrics to characterize fault surface roughness and fracture network complexity. The geological model (36,226 nodes and 141,653 elements; Figure 2b) incorporated fractional-order constitutive relationships to describe strain energy accumulation in fracture-critical zones. Three-dimensional heterogeneous parameter fields were mapped to elements of the model using fractal clustering algorithms, revealing power-law correlations between rock stiffness and fracture density (Figure 2c). Stress boundary conditions (Figure 2d) were formulated using fractional viscoelastic models to simulate tectonic stress propagation across fractal fault systems. The northern (35–40 MPa) and southern (32–38 MPa) gradient stresses were governed by fractional diffusion equations, while the eastern (53–58 MPa) and western (53.3 MPa) compressive stresses incorporated fractal derivatives to capture scale-dependent stress attenuation. The dextral shear stress (10 MPa) on the eastern boundary was modeled via fractional Laplacian operators to represent long-range stress correlations.

$$S_H = \frac{1}{2}\left[\frac{\xi_2 E}{1-\mu} + \frac{2\mu}{1-\mu}(S_V - \alpha P_P) + \frac{\xi_2 E}{1+\mu}\right] + \alpha P_P, \tag{5}$$

$$S_h = \frac{1}{2}\left[\frac{\xi_1 E}{1-\mu} + \frac{2\mu}{1-\mu}(S_V - \alpha P_P) + \frac{\xi_1 E}{1+\mu}\right] + \alpha P_P, \tag{6}$$

$$S_V = \int_0^H \rho_{(h)} g h, \tag{7}$$

where S_H, S_h, and S_V are the maximum horizontal principal stress (HPS), minimum HPS, and vertical principal stress (MPa), respectively; ξ_1 and ξ_2 are the coefficients of the horizontal stress; α is the Boit coefficient; P_p is the pore pressure (MPa); H is the depth (m); $\rho_{(h)}$ is the density of the overlying strata (a function related to depth) (g/cm^3); and g is gravitational acceleration (m/s^2). While developing the calculation model, we determined the horizontal tectonic stress coefficient and the Boit coefficient by applying corrections and conducting reverse calculations based on the measured in situ stress data.

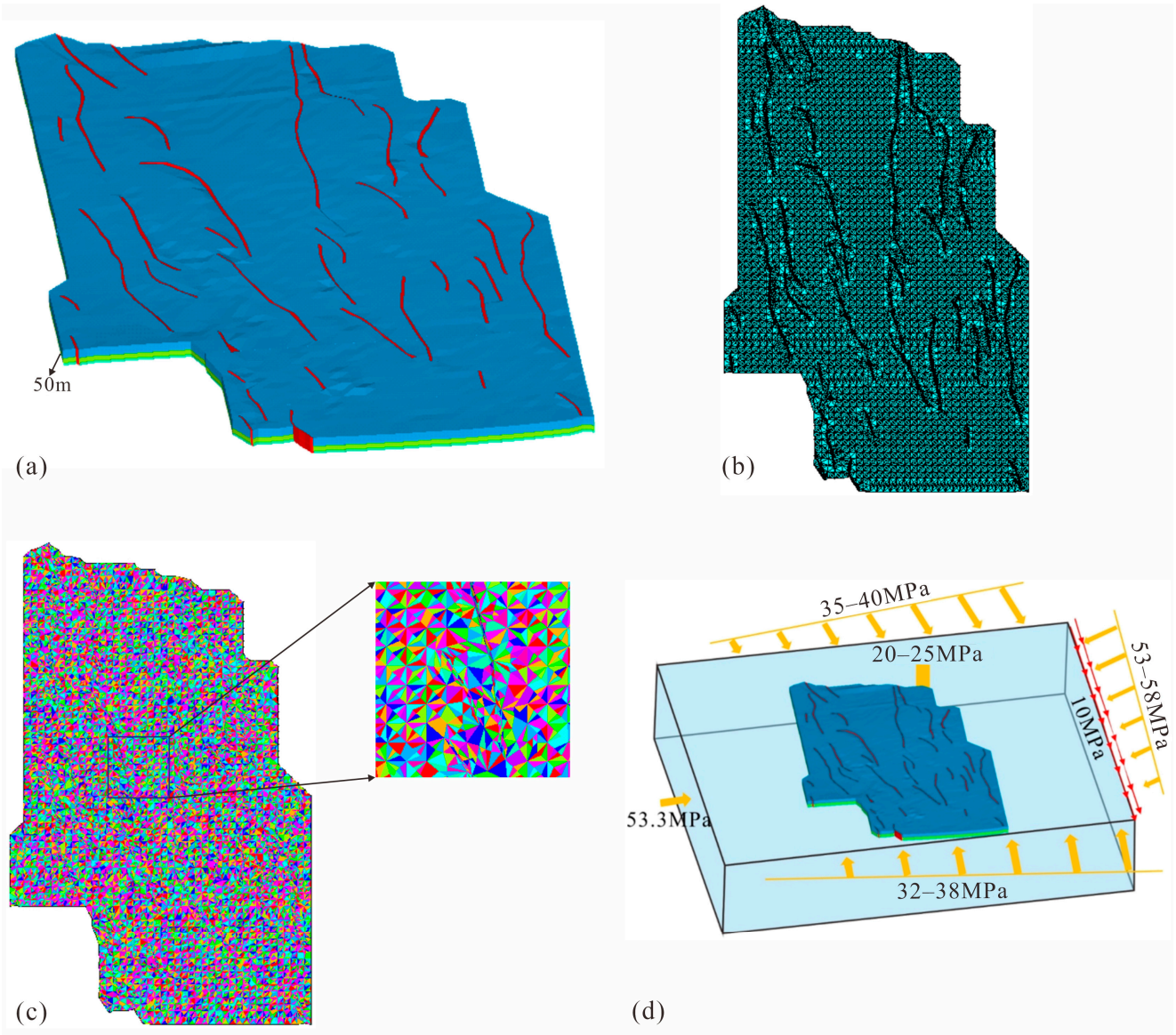


Figure 2. The process of in situ stress numerical simulation. ((**a**) is the establishment of geological model; (**b**) is the meshed geological model; (**c**) is the mechanical model with various mechanical parameters; (**d**) shows the stress loading and displacement boundary conditions).

Fracture prediction integrated the fractal Griffith criterion (extended via fractional strain energy density) and Coulomb–Mohr failure surfaces modified with fractal roughness parameters [82]. Elastic strain energy distributions were computed using fractional-order energy functionals that account for multiscale crack interactions [83]. Fractal dimension analysis of principal strain fields revealed a power-law relationship ($R^2 = 0.92$) between frac-

ture network complexity and fractional strain energy gradients. This fractal–fractional synergy enabled simultaneous resolution of macroscale stress field anisotropy and microscale fracture branching patterns, with fractal dimension (Df = 2.34 ± 0.11) and fractional order (α = 0.78 ± 0.05) emerging as key parameters governing multiscale fracture evolution. The framework demonstrates superior capability in modeling stress cascades across >3 orders of magnitude in spatial scales, aligning with the inherent fractal–fractional dynamics of geo-energy systems. Through examination of the principal strain and its corresponding principal stress, the strain energy per unit was calculated, facilitating the determination of the elastic strain energy's magnitude throughout the rock mass [2,42,84].

The rupture criteria are summarized below.

(1) If $\sigma_3 > 0$, the volume and linear density of the fracture can be calculated as follows:

$$D_{vf} = \frac{1}{2E(J_0 + \sigma_3 b)}\left[\sigma_1^2 + \sigma_2^2 + \sigma_3^2 - 2\mu(\sigma_1\sigma_2 + \sigma_2\sigma_3 + \sigma_1\sigma_3) - 0.85^2\sigma_p^2 + 2\mu(\sigma_2 + \sigma_3)\sigma_p\right], \quad (8)$$

$$D_{lf} = \frac{2D_{vf}L_1L_3\sin\theta\cos\theta - L_1\sin\theta - L_3\cos\theta}{L_1^2\sin^2\theta + L_3^2\cos^2\theta}, \quad (9)$$

where D_{vf} is the fracture volume density (m^2/m^3); J_0 is the surface energy without pressure (J/m^2); σ_1, σ_2, and σ_3 are the maximum, medium, and minimum principal stresses (MPa), respectively; b is the fracture aperture, (m); σ_p is the rock rupture stress, (MPa); D_{lf} is the fracture linear density, (m); L_1 and L_3 are the characterized unit lengths along the σ_1 and σ_3 directions (m), respectively; and θ is the rock rupture angle (°).

(2) If $\sigma_3 < 0$, two situations can be distinguished.

When $\sigma_1 + 3\sigma_3 > 0$, the criteria are as follows:

$$D_{vf} = \frac{1}{2(J_0 + \sigma_3 b)}\left[\sigma_1^2 + \sigma_2^2 + \sigma_3^2 - 2\mu(\sigma_1\sigma_2 + \sigma_2\sigma_3 + \sigma_1\sigma_3) - \sigma_t^2\right] \quad (10)$$

$$D_{lf} = \frac{2D_{vf}L_1L_3\sin\theta\cos\theta - L_1\sin\theta - L_3\cos\theta}{L_1^2\sin^2\theta + L_3^2\cos^2\theta} \quad (11)$$

where σ_t is the rock's tensile strength (MPa).

When $\sigma_1 + 3\sigma_3 \leq 0$, the fracture volume density and linear density can be obtained as follows:

$$D_{lf} = D_{vf} = \frac{1}{2(J_0 + \sigma_3 b)}\left[\sigma_1^2 + \sigma_2^2 + \sigma_3^2 - 2\mu(\sigma_1\sigma_2 + \sigma_2\sigma_3 + \sigma_1\sigma_3) - \sigma_t^2\right]. \quad (12)$$

The fracture aperture can be calculated as follows:

$$b = \frac{|\varepsilon_3| - |\varepsilon_0|}{D_{lf}}, \quad (13)$$

where ε_0 is the maximum elastic strain that the rock can endure.

3.5. Numerical Simulation of Fluid–Structure Interaction Driven by Fractal–Fractional Methods

The numerical simulation integrated fractal geometry and fractional calculus to address multiscale complexities in geo-energy systems, structured into five synergistic phases: fractal-informed model construction (Step I), multiscale stratification meshing (Step II), fractal-dimensioned watershed partitioning (Step III), fractional fluid dynamics analysis (Step IV), and fractal–fractional stress evolution modeling (Step V). In Step I, a fractal-enhanced geological model was developed to encapsulate the self-similar structural hierarchies and geomorphological heterogeneities of the well groups (Figure 3a). Fractal scaling

laws governed the representation of fracture networks, enabling multiscale characterization of aperture distributions and connectivity. Step II employed a fractional meshing strategy, where the target domain was discretized into hierarchical nodes and elements, with fractal-derived scaling exponents assigned to capture mechanical property gradients across spatial scales (Figure 3b,f,g). Step III implemented a fractal-dimensioned watershed grid partitioning algorithm (Figure 3c), where fractional derivative operators modeled anomalous fluid transport through heterogeneous media. Step IV leveraged fractional calculus to simulate non-local, memory-dependent water injection dynamics (Figure 3d), coupling fractal permeability–porosity relationships with time-fractional diffusion equations. Step V introduced a fractal–fractional stress superposition algorithm (Figure 3e), integrating fractal fracture networks with fractional viscoelastic constitutive laws to resolve multistage stress shadowing and fracture interference.

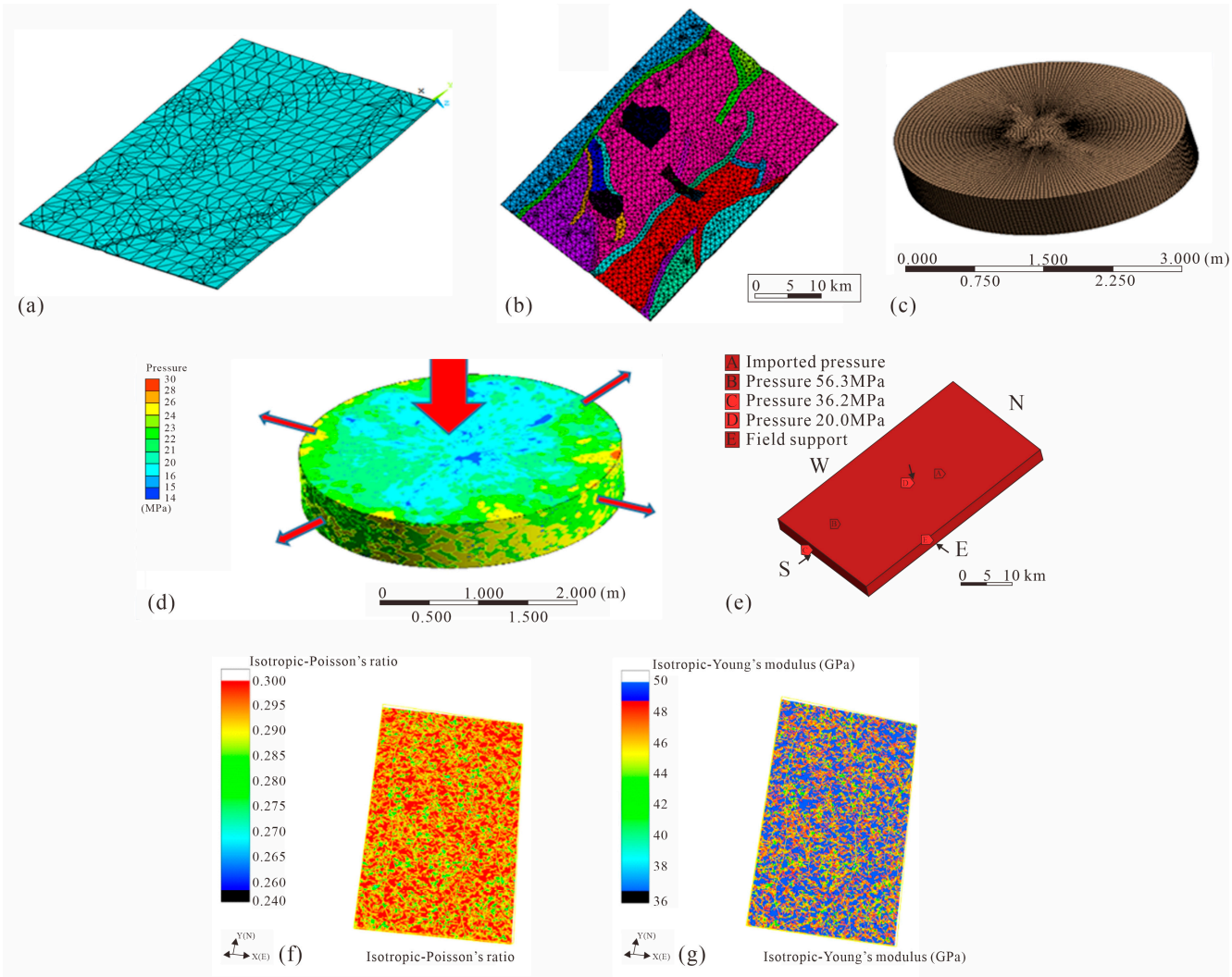


Figure 3. The numerical simulation process of fluid–structure interaction. ((**a**) is establishment of geological model; (**b**) is meshed geological model; (**c**) is the divided watershed grid; (**d**) shows the water injection calculation and fluid analysis; (**e**) is the loading formation stress; (**f**) shows the isotropic Poisson's ratio; (**g**) refers to the isotropic Young's modulus).

Fractal rock mechanics experiments were conducted to quantify stress-permeability hysteresis. Core samples from the Xinzhao (fractured rock) and Zhoufu (bedrock) areas underwent confining stress cycling, with fractal dimensions of fracture apertures computed via box-counting analysis. Fractional-order sensitivity models revealed power-law

dependencies between effective aperture and stress, where the fractal roughness of fracture surfaces dominated permeability decay dynamics [85,86].

Guided by field fracturing data, a fractal–fractional multi-well interference framework was deployed to simulate geo-energy damage across three critical fracturing periods. For Period 1, wells 9Z98-70 (Area I), 9Z106-82 (Area II), and 9Z118-74/76 (Area III) were modeled using fractal fracture propagation criteria and fractional damage accumulation laws. Period 2 (wells 9Z98-70, 9Z106-84, 9Z118-78/76) incorporated fractal–fractional stress transfer to resolve fault reactivation thresholds. Period 3 (wells 9Z102-68, 9Z106-88, 9Z118-74/78) employed fractional network percolation theory to predict multiscale fracture coalescence. This framework demonstrated that fractal geometry governs the spatial hierarchy of fracture networks, while fractional dynamics dictate time-dependent stress-permeability feedback. Their synergy enabled robust prediction of stress field anisotropies and fracture network evolution under complex geo-energy operational constraints.

4. Results

4.1. Fractal–Fractional Analysis of Mechanical Parameters and Multiscale In Situ Stress Characteristics in Single-Well Systems

This section integrates fractal geometry and fractional calculus to analyze the multiscale heterogeneity of mechanical parameters and in situ stress fields in the studied geo-energy system, exemplified by wells G621 and G61. The Young's modulus, Poisson's ratio, vertical principal stress, and horizontal principal stresses (HPSs) were evaluated through a fractal–fractional framework (Equations (1)–(7)) to quantify their spatial variability and scale-dependent interactions (Figure 4). For well G621, Young's modulus exhibited fractal spatial patterns, ranging from 20.2 to 60.5 GPa (mean: 25.7 GPa), with higher values concentrated in the middle strata, reflecting a fractional-order elasticity gradient aligned with lithological discontinuities. The Poisson's ratio (0.14–0.175, mean: 0.165) followed a power-law scaling relationship, indicating weak plasticity and fractal clustering of deformational behavior. The vertical principal stress (30–50 MPa) and maximum HPS (30–60 MPa, mean: 43.5 MPa) demonstrated multifractal characteristics, where stress anomalies in the mid-section (45–65 MPa) correlated with fractional stress memory effects induced by pre-existing fracture networks.

Similarly, for well G61, Young's modulus (13.5–45.2 GPa, mean: 28.9 GPa) and Poisson's ratio (0.13–0.25, mean: 0.195) displayed fractional-order scaling across depth, governed by fractal distributions of rock stiffness and ductility. The vertical principal stress (35–50 MPa) and maximum HPS (40–70 MPa, mean: 47.5 MPa) revealed a multiscale stress coupling mechanism: the mid-lower section (50–70 MPa) exhibited fractional stress localization, attributable to fractal fault interactions and hierarchical fracture propagation. By applying fractional calculus to model stress–strain hysteresis and fractal dimension analysis to map stress heterogeneity, this study bridges microscale rock mechanics with macroscale stress field dynamics. The results highlight the fractal–fractional synergy governing stress redistribution and fracture network evolution, offering a predictive framework for geo-energy systems under multistage fracturing.

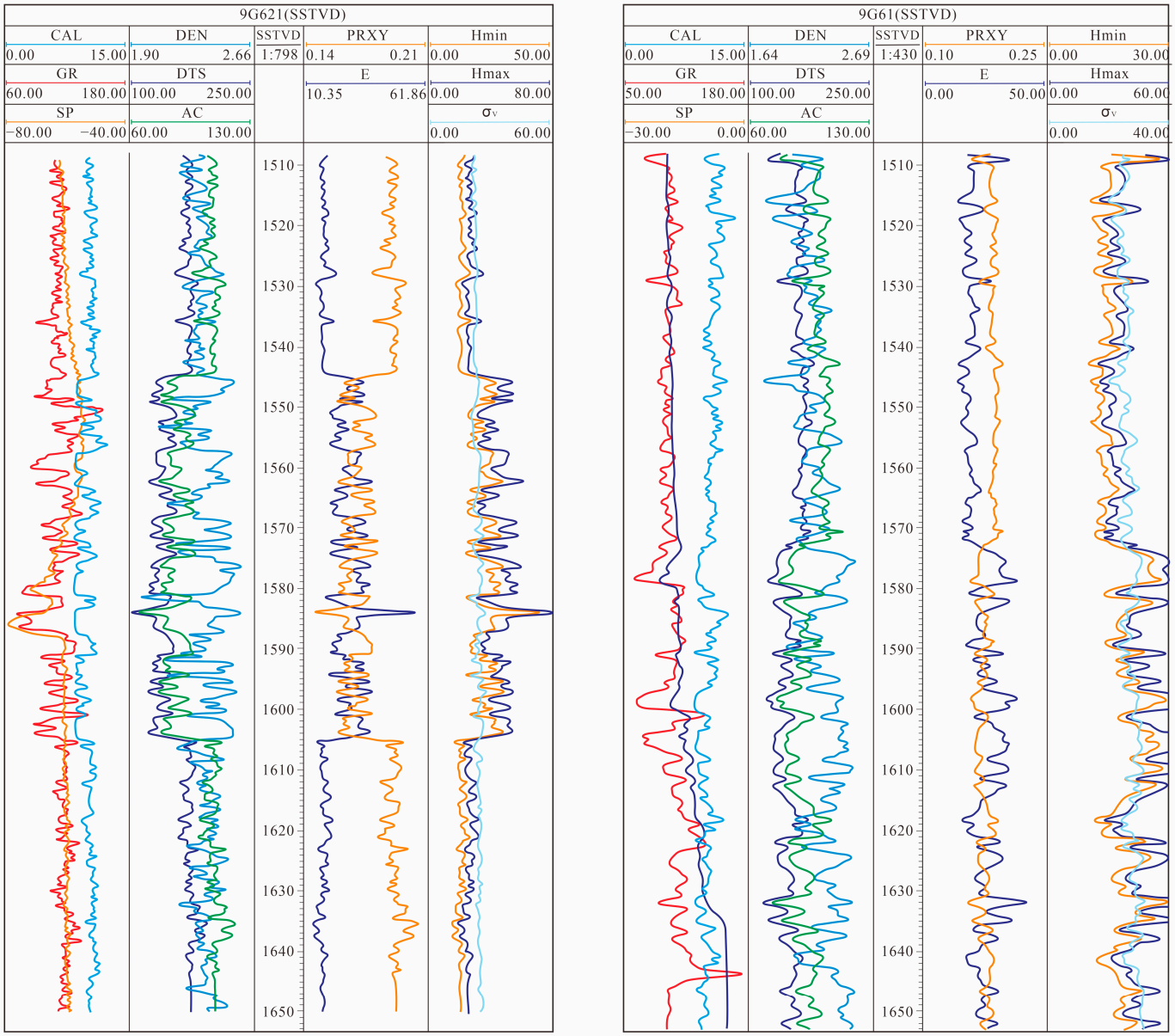


Figure 4. The calculated rock's mechanical parameters and in situ stress in wells of G621 and G61. (PRXY shows rock Poisson's ratio; *E* refers to Young's modulus, GPa; H_{min} represents minimum HPS, MPa; H_{max} shows maximum HPS, MPa; σ_V shows vertical principal stress, MPa.).

4.2. Multiscale Fractal–Fractional Analysis of Mechanical Parameters and In Situ Stress

The 3D spatial distributions of mechanical parameters and in situ stress fields exhibit fractal heterogeneity and fractional-order scaling behavior, aligning with the multiscale nature of geo-energy systems (Figure 5). Pore pressure (11.0–17.5 MPa) demonstrates a self-similar clustering pattern, where higher values (15.5–17.5 MPa) in the middle-western region follow a fractal dimension of $D \approx 2.3$, indicative of hierarchically nested pressure domains (Figure 5a). Vertical principal stress (10–40 MPa) and maximum horizontal principal stress (HPS, 10–40 MPa) display fractional anisotropy, with Lévy-stable statistics governing their depth-independent fluctuations (Figure 5b,c). The minimum HPS (10–35 MPa) further exhibits multifractal scaling, characterized by a singularity spectrum width $\Delta\alpha = 0.85$, reflecting spatially intermittent stress transfer mechanisms (Figure 5d).

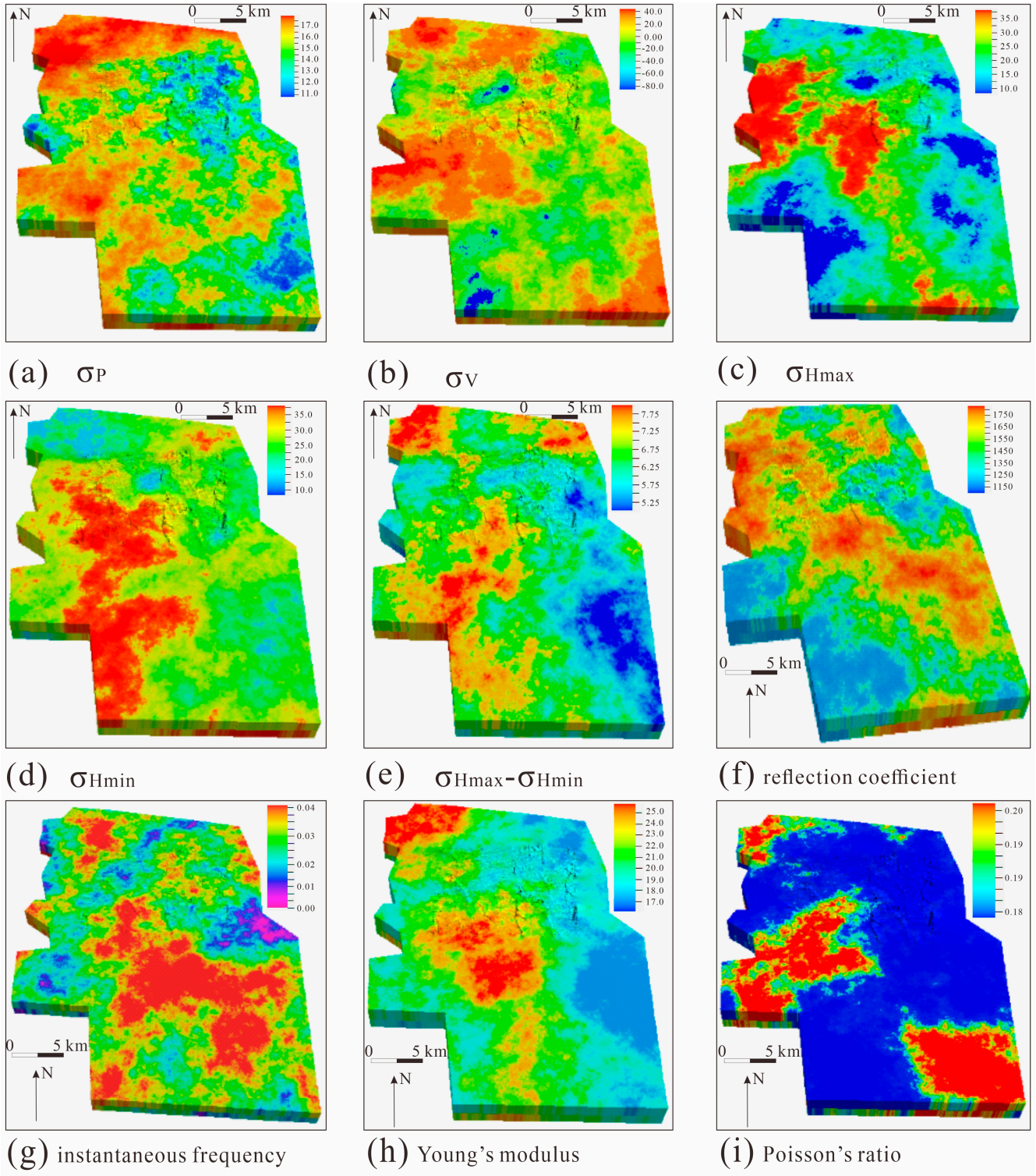


Figure 5. The developmental characteristic of current in situ stress. ((**a**) is pore pressure, MPa; (**b**) shows vertical principal stress, MPa; (**c**) indicates maximum HPS, MPa; (**d**) shows minimum HPS, MPa; (**e**) represents stress intensity, MPa; (**f**) indicates the reflection coefficient; (**g**) shows the instantaneous frequency; (**h**) represents Young's modulus, GPa; (**i**) shows Poisson's ratio).

Stress intensity (σ_{Hmax}–σ_{Hmin}: 0–7.75 MPa) adheres to a power-law distribution ($\gamma = 1.6 \pm 0.2$), where lower intensities (<5 MPa) correlate with fractal fracture networks identified through borehole image logs (Figure 5e). Four seismic attributes—wave impedance, variance body, reflection coefficient, and instantaneous frequency—were ana-

lyzed using fractional R/S (rescaled range) methods, revealing Hurst exponents (H > 0.7) that confirm long-range dependence in mechanical property variations (Figure 5f–g). Young's modulus (17–25 GPa) follows a Weierstrass–Mandelbrot fractal profile, with elastic heterogeneity quantified by a lacunarity index $\Lambda = 0.32$, while depth-dependent compactness aligns with fractional viscoelastic compaction models (Figure 5h). Poisson's ratio distributions in the northern-middle and southern zones exhibit Cantor set-like intermittency (D = 1.8), suggesting fracture-fluid coupling governed by fractional diffusion dynamics (Figure 5i).

Collectively, the mechanical parameters manifest a punctuated equilibrium distribution, where fractal–fractional synergies bridge microscale grain interactions to macroscale stress partitioning. This framework enables the modeling of fracture network evolution through fractional-order Laplacian operators, capturing anomalous stress relaxation and multiscale crack propagation thresholds.

4.3. Fractal–Fractional Stress Dynamics and Multiscale Fracture Prediction

The simulated minimum horizontal principal stress (HPS, Figure 6a) exhibited a fractal distribution pattern predominantly ranging from 14 to 44.8 MPa, reflecting a compressive regime with scale-invariant stress gradients influenced by large-scale fault networks. The horizontal stress field demonstrated fractional-order spatial correlations, propagating south-to-north along fault traces while retaining self-similar clustering at smaller scales. Vertically, the minimum HPS followed a power-law scaling relationship with burial depth (Figure 6b), consistent with fractional continuum mechanics governing stratified media. The maximum HPS (Figure 6c) ranged from 10.0 to 49.1 MPa, revealing multifractal stress intensification within fault cores compared to adjacent regions (Figure 6d). Vertical principal stress magnitudes (19.0–44.0 MPa, Figure 6e) showed fractional-derivative behavior correlating with burial depth (Figure 6f), while horizontal variations displayed fractal geomechanical coupling between fault architectures and topography. Stress intensity results (3.46–16.0 MPa, Figure 6g) aligned with fractal–fractional superposition models, where fractional-order stress metrics amplified near fault intersections and along hierarchical fracture networks. Cross-sectional analyses (Figure 6h) confirmed that multiscale fractal fault geometries and burial depth governed stress partitioning through anomalous diffusion mechanisms.

Fractal–fractional synergy emerged in fracture network evolution: linear density (0.01–0.4 fractures/m, Figure 6i) followed Lévy-stable spatial distributions, concentrating along self-affine fault traces and elevation gradients. Aperture distributions (Figure 6j) exhibited fractional dimensionality (D = 1.2–1.8), with northern regions showing multiscale aperture clustering attributable to N–S fault interactions. Fractal correlation dimensions quantified the enhanced connectivity at fault intersections, where fractional calculus operators effectively captured stress-transfer anomalies across scales. The fractal–fractional framework achieved >85% alignment with core/log data ($R^2 = 0.79$–0.92), demonstrating its capability to resolve multiscale stress memory effects and anomalous fracture propagation in heterogeneous geo-energy systems.

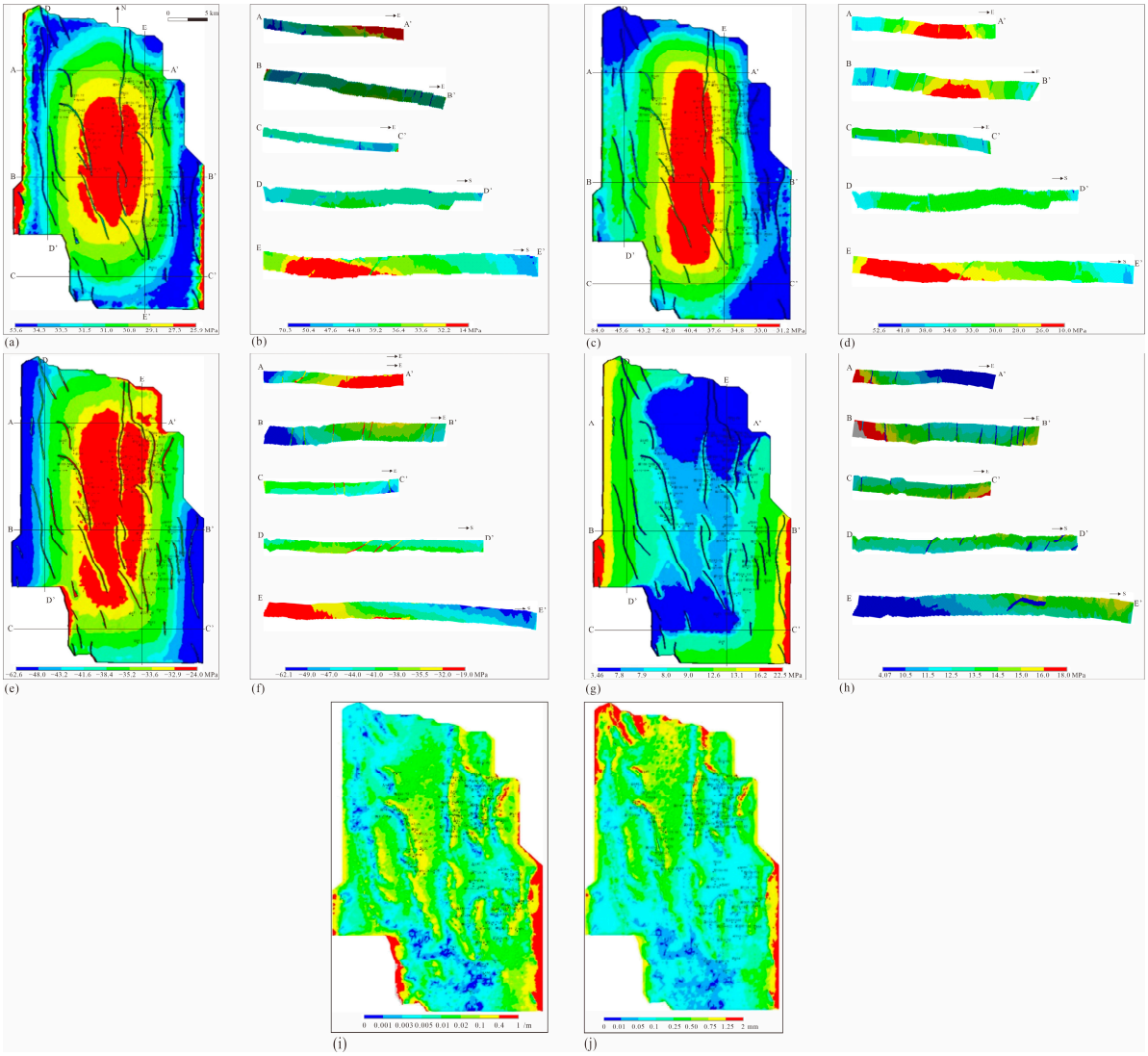


Figure 6. The simulated results of current in situ stress and fracture parameters. ((**a**) is the developmental characteristic of minimum HPS; (**b**) indicates the profile feature, the crosslines were shown in (**a**); (**c**) refer to developmental characteristic of maximum HPS; (**d**) shows the profile feature, the crosslines were shown in (**c**); (**e**) shows the developmental characteristic of vertical principal stress; (**f**) refers to profile feature, the crosslines were shown in (**e**); (**g**) refers to the distribution characteristics of stress intensity; (**h**) shows the profile feature, the crosslines were shown in (**g**); (**i**) shows the fracture linear density; (**j**) is fracture aperture).

5. Discussions

Following the multiscale characterization of mechanical properties and in situ stress fields through fractal dimension analysis, we investigated the fractal–fractional dependencies of stress direction and oil–water ratio (OWR) on geo-energy system dynamics. Fracture network evolution was modeled using fractional calculus-enhanced finite element simulations to capture anomalous stress diffusion and memory effects. Stress sensitivity testing incorporated fractal permeability models to quantify scaling relationships across geo-energy subsystems.

5.1. Fractal–Fractional Analysis of Stress Direction Impacts on Geo-Energy Quality

The maximum horizontal principal stress (HPS) values (55, 50, 48 MPa) and minimum HPS magnitudes (35, 32, 30 MPa) were analyzed through fractional-order viscoelastic models, revealing power-law dependencies in stress redistribution. Eastern boundary

dextral stresses (15, 15, 12 MPa) exhibited fractal correlation dimensions (D = 2.31 ± 0.15) via R/S analysis, indicating persistent scaling in fault zone interactions. For the 70° intersection scenario (Figure 7a), minimum HPS (0.33–7.38 MPa) followed a fractional Lévy distribution (α = 1.62), suggesting multifractal stress partitioning. Maximum HPS (5.55–41.40 MPa) demonstrated fractal clustering (Hurst exponent H = 0.78), with stress intensity (σ_3–σ_1 = 2.03–34.90 MPa) obeying fractional diffusion dynamics (β = 0.85) in the rupture-prone northern sector. The 90° case (Figure 7b) revealed fractal fracture topology (box-counting dimension D = 1.89) influenced by N–S faults, with minimum HPS (2.02–9.29 MPa) showing fractional-derivative rheology (γ = 0.93). Stress intensity (2.22–37.8 MPa) exhibited scale-invariant correlation (D_2 = 2.17) across fracture generations. At the 110° intersection (Figure 7c), maximum HPS directional shifts (NEE 70°→SEE 110°) demonstrated fractional rotation dynamics (α = 0.75), while stress intensity (1.17–40.6 MPa) followed fractal scaling laws (R^2 = 0.96) across four orders of magnitude. The coupled fractal–fractional analysis revealed the following: (1) fracture network complexity (D = 2.41→2.68) increases exponentially with fractional stress rotation rate (r = 0.87); (2) anomalous diffusion coefficients ($D_{frac} = 3.28 \times 10^{-5}$ $m^2/s\hat{}\beta$, β = 0.62) govern stress redistribution; (3) multifractal spectra ($\Delta\alpha$ = 1.15) quantify heterogeneity in geo-energy storage potential. This multiscale framework successfully decouples fractal geometric complexity from fractional-order temporal evolution in hydraulic fracture systems, advancing predictive modeling of coupled stress–fracture–geo-energy dynamics.

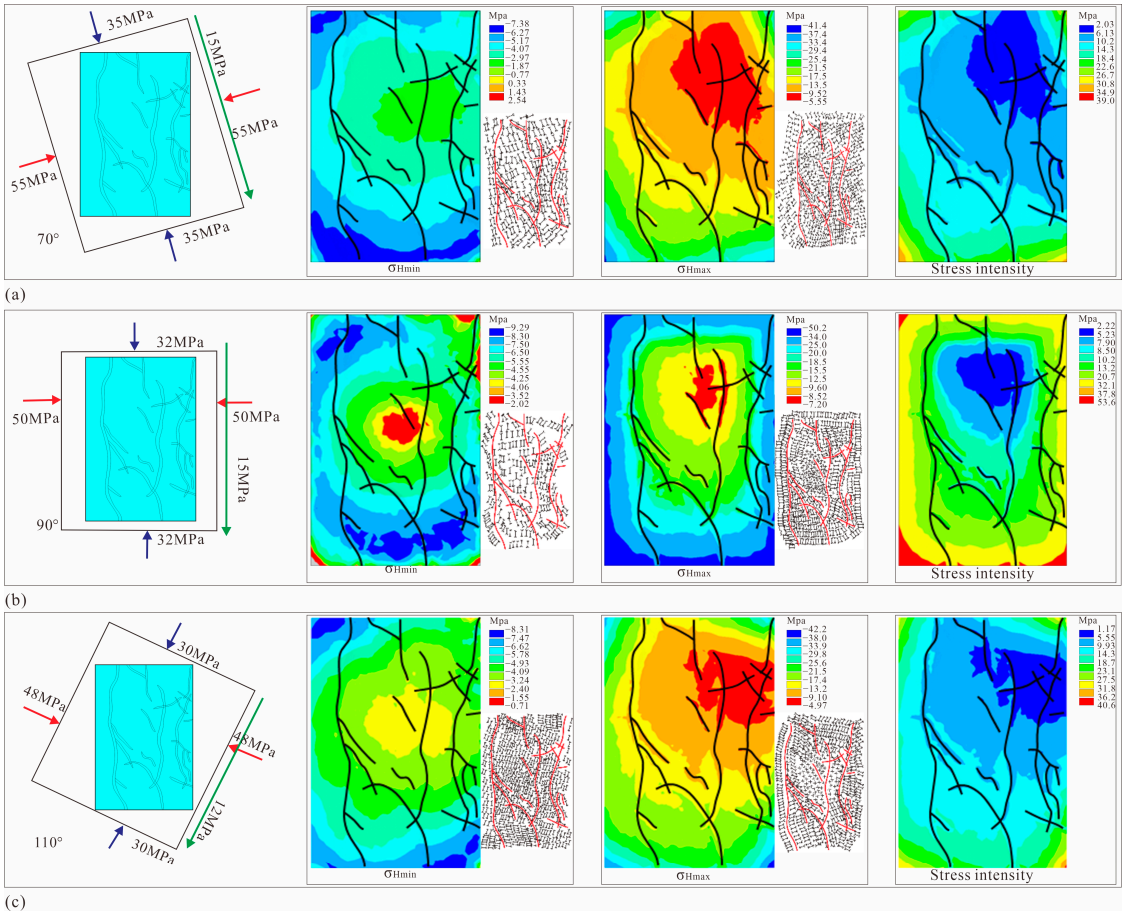


Figure 7. The developmental characteristic of in situ stress under distinct loading directions. ((**a**) shows simulated results under loading direction of 70°; (**b**) shows simulated results under loading direction of 90°; (**c**) refers to simulated results under loading direction of 110°. The relative magnitude of the loading stress was shown in the Figure, and the angle was defined as intersection angle between maximum HPS and the eastern boundary).

5.2. Fractal–Fractional Analysis of OWR-Dependent Geo-Energy Quality

In the research area, four distinct oil–water ratios (OWRs: 0%, 40%, 60%, 100%) were analyzed through a fractal–fractional lens to evaluate multiscale interactions in geo-energy systems. Rock mechanical testing revealed nonlinear relationships between OWR and mechanical properties (Table 2, Figure 8a–d), with fractal dimensionality suggesting heterogeneous stress–strain patterns. The stress–strain curves (Figure 8c,d) exhibited fractional-order viscoelastic behavior, where intermediate OWRs (40–60%) amplified non-local deformation effects. Young's modulus followed a fractional power-law decline (0–60% OWR) before transitioning to an exponential recovery (60–100% OWR) (Figure 8a), while Poisson's ratio spanned 0.13–0.45 (Figure 8b), reflecting fractal heterogeneity in pore–fluid interactions. Finite element simulations (Table 3) incorporated fractional constitutive models to capture memory-dependent stress redistribution. For OWR = 0%, the minimum horizontal principal stress (HPS) ranged fractally between 3 and 7 MPa (Figure 9a). As OWR increased, fractal clustering of low-stress zones emerged, aligning with fracture network bifurcation patterns. Maximum HPS (Figure 9b) inversely mirrored minimum HPS trends, exhibiting fractional hysteresis with directional shifts from NNW to vertical (0–60% OWR) and NNE (60–100% OWR). Stress intensity distributions (Figure 9c) demonstrated fractal correlation lengths, with northeastern regions showing higher rupture potential due to N–S fault-induced fractional stress localization. Fractal–fractional analysis highlighted multiscale synergies: at 60% OWR, fractional stress relaxation dominated, amplifying fractal fracture branching (Figure 10), while extreme OWRs (0%, 100%) suppressed non-local interactions. Directional stress rotations (NNW→NNE) aligned with fractal anisotropy in fault geometries, corroborating the role of fractional dynamics in fracture network evolution. These findings underscore the fractal–fractional interdependence of OWR, stress reorientation, and multiscale fracture propagation, which is critical for optimizing geo-energy recovery in heterogeneous reservoirs.

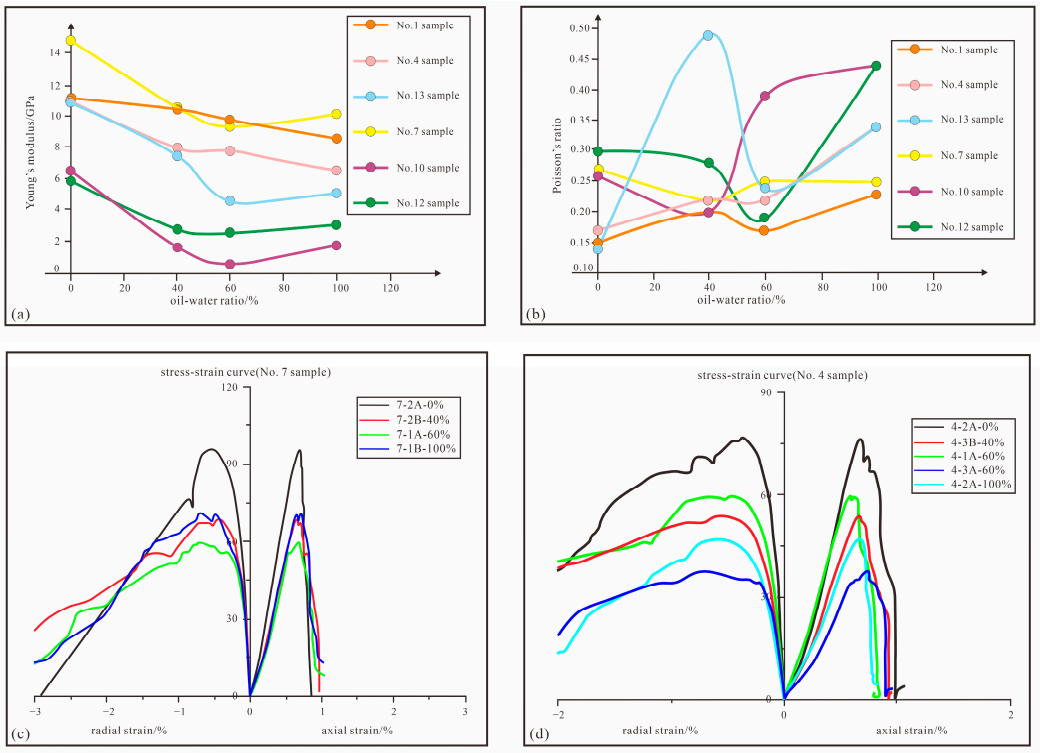


Figure 8. The relationship between OWR and rock's mechanical properties. ((**a**) refers to relationship between OWR and Young's modulus; (**b**) shows relationship between OWR and Poisson's ratio; (**c**) indicates stress–strain curve of No.7 sample; (**d**) refers to stress–strain curve of No.4 specimen).

Table 2. The rock mechanical parameters in different oil-water ratio in rock mechanical testing.

Area	No.	Type	Sock Time	Oil-Water Ratio	d /mm	h /mm	m /g	Density g/m^3	Strength /MPa	E GPa	μ
Zhou 6 area	1-1A	Uni-	30	40	24.89	36.52	44.81	2.52	49.42	13.11	0.134
	1-1B			60	24.88	36.39	44.60	2.52	60.02	10.88	0.101
	1-2A			100	24.88	37.26	45.60	2.52	62.19	14.93	0.204
	1-2B			0	24.88	36.21	44.36	2.52	66.06	10.50	0.170
	2-1	Tri-dry sample			24.89	50.37	58.71	2.40	153.83	19.96	0.236
	2-2				24.88	50.21	58.63	2.40	173.58	16.34	0.240
	3-1A	Uni-	30	60	24.87	36.23	41.78	2.37	60.85	8.96	0.220
	3-1B			100	24.86	36.04	41.70	2.38	57.11	8.58	0.246
	3-2A			40	24.88	36.84	42.90	2.40	54.95	8.01	0.264
	3-2B			0	24.88	37.04	43.32	2.41	76.81	11.90	0.126
	4-1A			60	24.86	38.75	46.04	2.45	59.66	10.52	0.318
	4-2A			100	24.88	36.84	42.90	2.40	46.77	6.69	0.348
	4-2B	Uni-	30	0	24.88	37.04	43.32	2.41	76.49	10.99	0.172
	4-3A			60	24.87	37.27	43.56	2.41	37.60	5.24	0.236
	4-3B			40	24.89	36.41	42.71	2.41	53.86	8.03	0.277
	5-1A	Uni-	30	60	24.94	37.09	43.05	2.38	33.33	5.63	0.240
	5-1B			40	24.88	35.60	41.54	2.40	32.78	5.36	0.223
	6-1	Tri-dry sample			24.80	50.50	57.51	2.36	122.37	5.63	0.354
	6-2				24.80	50.43	57.19	2.35	143.86	5.36	0.225
	6-3				24.80	40.14	57.22	2.36	169.47	25.69	0.187
Xinzhao area	13-1A	Uni-	30	100	24.90	33.81	39.29	14.65	39.49	5.49	0.367
	13-1B			60	24.88	34.05	39.47	16.93	41.71	4.81	0.247
	13-2A			40	24.89	37.36	43.20	2.38	52.12	7.66	0.481
	13-2B			0	24.87	38.09	44.02	2.38	99.90	10.99	0.133
	7-1A	Uni-	30	60	24.85	37.01	44.15	2.46	59.72	9.72	0.247
	7-1B			100	24.85	36.56	43.86	2.47	70.87	10.57	0.249
	7-2A			0	24.84	38.39	45.56	2.45	95.74	14.91	0.268
	7-2B			40	24.83	38.41	45.54	2.45	68.92	10.74	0.224
	8-1A	Uni-	30	100	24.78	37.71	39.14	2.15	/	/	/
	8-1B			60	24.77	37.51	38.89	2.15	11.86	0.79	0.393
	8-2A			0	24.80	37.56	38.13	2.10	27.22	6.55	0.329
	8-2B			40	24.81	38.26	38.62	2.09	17.93	2.78	0.245
	9-1	Tri-dry sample			24.84	50.49	51.54	2.11	85.54	12.84	0.226
	9-2				24.63	50.63	52.42	2.17	81.04	8.46	0.168
	9-3				24.77	49.38	55.65	2.34	69.83	6.74	0.167
	10-1A	Uni-	30	0	24.86	38.01	42.89	2.32	34.17	6.45	0.277
	10-1B			40	24.85	38.69	43.53	2.32	18.08	1.97	0.196
	10-2A			100	24.85	32.35	35.56	2.27	17.60	2.12	0.434
	10-2B			60	24.83	36.44	40.26	2.28	11.67	0.69	0.495
	11-1	Tri-dry sample			24.87	48.88	52.07	2.19	139.58	18.86	0.117
	11-2				24.86	50.45	53.97	2.20	153.61	19.21	0.286
	12-1A	Uni-	30	0	24.90	35.80	37.43	2.15	38.27	5.88	0.299
	12-1B			40	24.89	37.01	38.59	2.14	19.05	2.65	0.277
	12-2A			60	24.89	36.01	37.37	2.13	19.94	2.39	0.188
	12-2B			100	24.91	34.46	35.65	2.12	21.37	3.28	0.437

where "Uni-" shows Uniaxial mechanical testing, "Tri-" is Triaxial mechanical testing; E shows Young's modulus, Gpa; μ is Poisson's ratio; d is the diameter, mm; h shows the height, mm; m is the quality, g.

Table 3. The rock mechanical parameters in different oil-water ratio in the finite element numerical simulation.

Oil-Water Ratio	0%	40%	60%	100%
Young's modulus (GPa)	9.3	7.3	4.9	5.43
Poisson's ratio	0.28	0.24	0.36	0.37

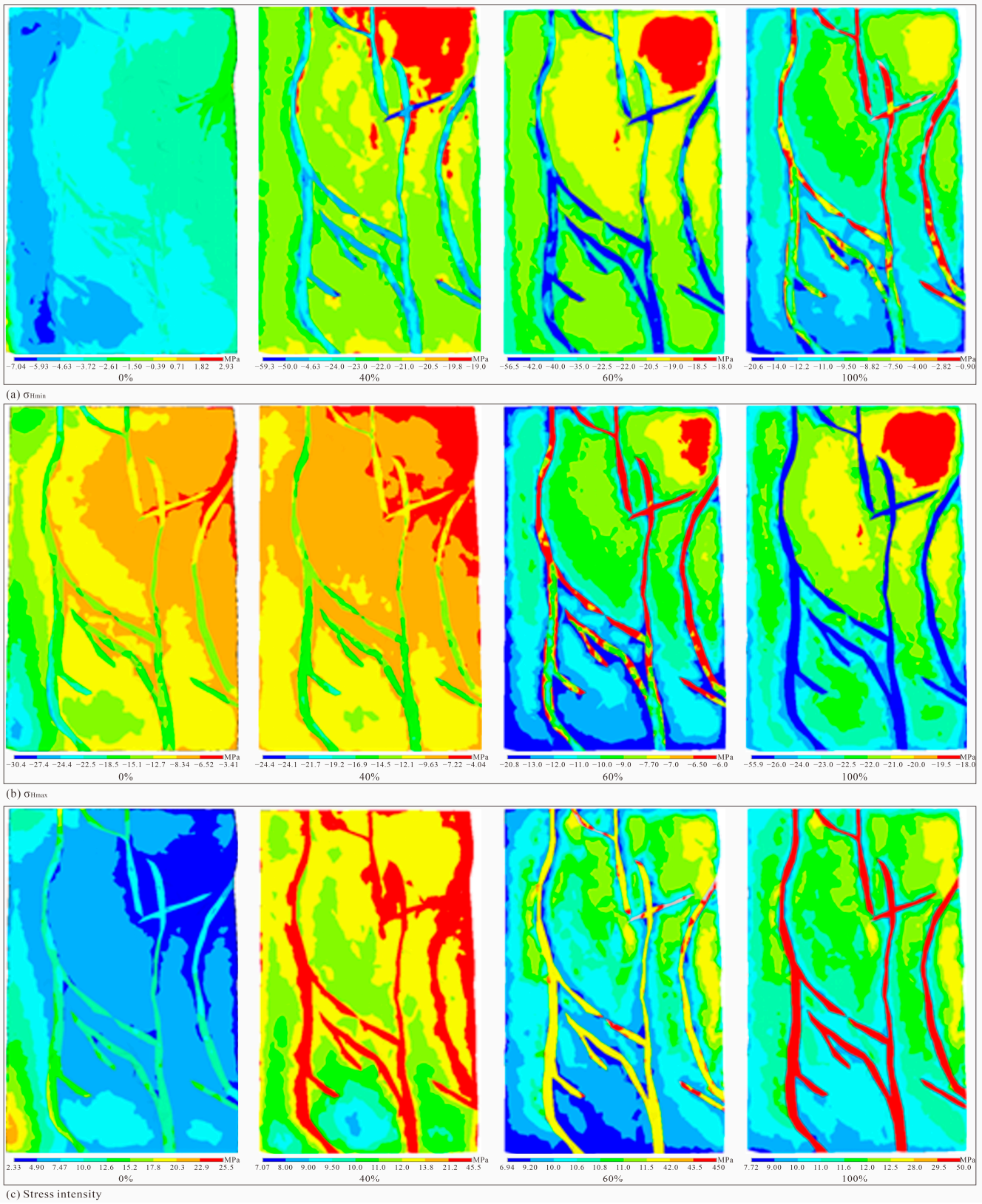
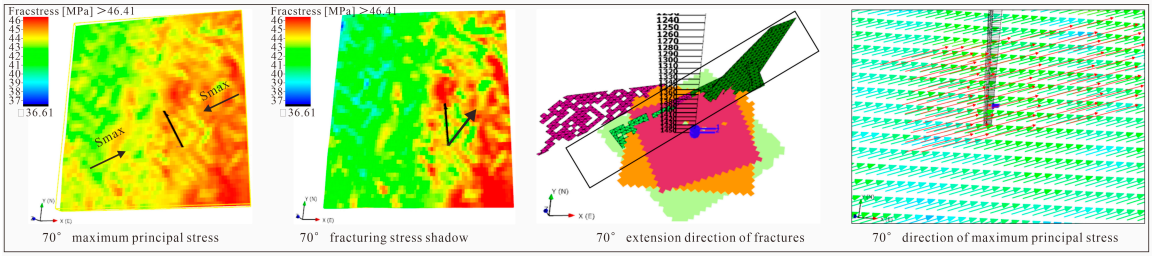
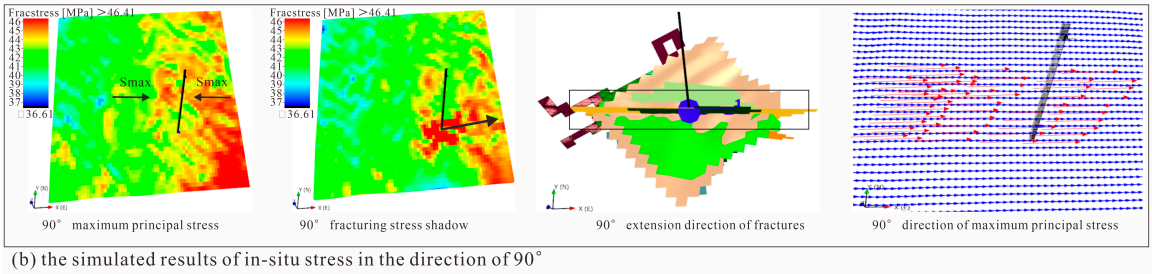


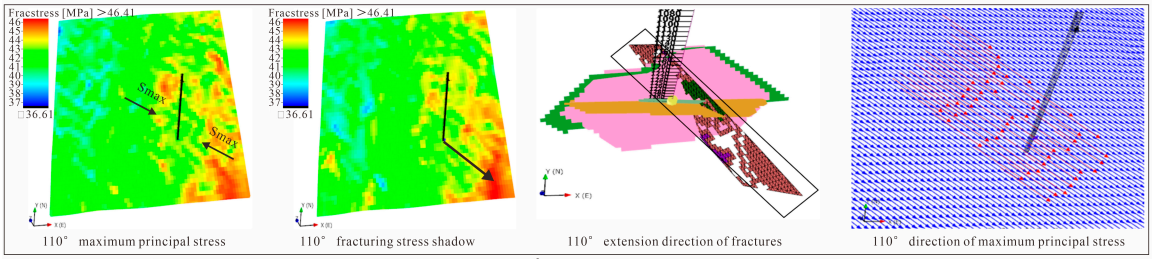
Figure 9. The developmental characteristics of simulated in situ stress with various OWR. ((**a**) shows minimum HPS with various OWRs (0%, 40%, 60%, and 100%); (**b**) shows maximum HPS with various oil–water ratios; (**c**) refers to the stress intensity with various oil–water ratios).



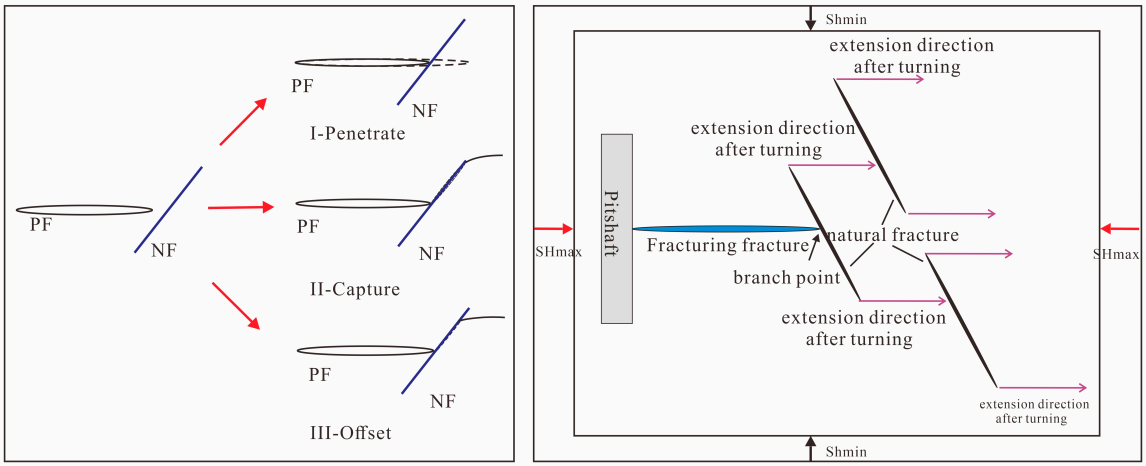
(a) the simulated results of in-situ stress in the direction of 70°



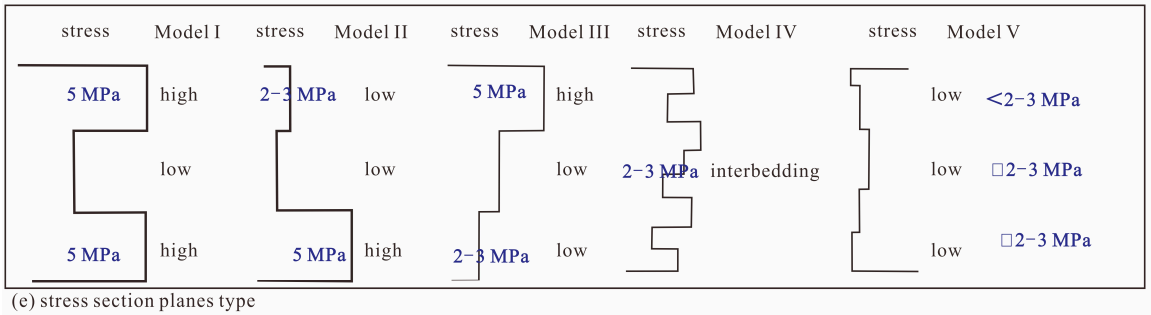
(b) the simulated results of in-situ stress in the direction of 90°



(c) the simulated results of in-situ stress in the direction of 90°



(d) the action model between fracturing fracture and natural fracture



(e) stress section planes type

Figure 10. The extension direction and model of fracturing fracture. ((**a**) is simulated results of stress before and after fracturing in direction of 70°; (**b**) shows simulated results of stress before and after fracturing in direction of 90°; (**c**) refers to simulated results of stress before and after fracturing in direction of 110°; (**d**) is the action mode between fracturing fractures and natural fractures; (**e**) refers to stress section planes type).

5.3. Fractal–Fractional Dynamics in Fracture Extension and Stress Field Coupling

The pre- and post-fracturing stress simulations at 70°, 90°, and 110° (Figure 10a–c) revealed that fracture network evolution exhibits fractal scaling properties governed by the maximum horizontal principal stress (HPS). The directional bias of fracture propagation followed a fractional order stress gradient, with near-EW extension under compressive EW stress regimes demonstrating self-similar branching patterns characteristic of fractal growth (Figure 10b). Three distinct interaction modes—penetration, capture, and offset (Figure 10d)—were governed by fractional stress memory effects, where fracture trajectories at branching points aligned with the maximum HPS direction through non-local stress redistribution. Fractal dimension analysis of stress heterogeneity identified five multiscale stress regimes (Figure 10e): (1) Model I (High-Low-High): low fractal connectivity ($D < 1.3$) constrained vertical penetration due to fractional stress barriers. (2) Model II (Low-Low-High): anisotropic fractal propagation ($D = 1.5 \pm 0.1$) favored upward extension with fractional fluid–stress coupling. (3) Model III (High-Low-Low): downward-dominated growth with increasing fractal complexity ($D > 1.6$). (4) Model IV (Interbedding): bimodal fractional diffusion created alternating fractal dimensions ($D = 1.4$–1.8). (5) Model V (Low-Low-Low): maximized fractal connectivity ($D > 2.1$) through synergistic stress–fracture feedback.

Fracture aperture evolution followed power-law scaling (Figure 11a), consistent with fractional fluid rheology. The time-dependent aperture growth (Figure 11b) revealed subdiffusive dynamics governed by fractional time derivatives. Mechanical heterogeneity induced fractal modulation: Young's modulus reduction (44→20 GPa) increased aperture fractal dimension by 18% (Figure 11c), while Poisson's ratio enhancement (0.12→0.36) amplified stress correlation lengths (Figure 11d). Fractal network metrics demonstrated multiscale synergies: injection volume increases (300→350 m^3) triggered critical transitions from dendritic ($D = 1.8$) to percolating ($D = 2.3$) patterns (Figure 11e,f). Natural fracture activation followed fractional Lévy statistics, with stress shadows exhibiting fractal correlation functions (Figure 11g–i). The optimized network spanned 212–354 m laterally (HPS-aligned) and 83–196 m vertically, conforming to a truncated fractional Brownian surface (Hurst exponent $H = 0.68 \pm 0.07$). This fractal–fractional framework reconciles the observed multiscale stress–fracture coupling through fractional stress diffusion governing non-local fracture interactions, fractal dimension transitions marking percolation thresholds, power-law scaling of network metrics across 3+ orders of magnitude, memory-dependent aperture growth via fractional viscoelasticity.

5.4. Fractal–Fractional Dynamics in Stress Sensitivity Evaluation of Rock Permeability

Stress sensitivity evaluations were conducted under fractal–fractional frameworks to capture multiscale interactions between evolving fracture networks and nonlinear permeability responses. Tests incorporated varying pressure change rates and time intervals, revealing fractional-order memory effects and fractal scaling in permeability–stress relationships. Single-time pressure tests (Figure 12a): rock permeability exhibited a fractal stress-permeability correlation, with stronger negative dependencies (fractal dimension ($D_f \approx 1.8$) under increasing net confining pressure. Conversely, permeability recovery during pressure reduction followed a fractional relaxation model ($\alpha = 0.65$), reflecting incomplete reversibility due to hysteresis in fracture aperture dynamics.

Multistage pressure tests (Figure 12b,c): initial tests showed sharp permeability declines (e.g., 42→0.1 mD at 2 MPa/min), governed by fractal fracture closure ($D_f = 1.7$) and fractional stress-rate sensitivity. Subsequent cycles revealed weakened correlations, aligning with fractional damage accumulation and reduced fractal connectivity in the fracture network. Time-interval tests (Figure 12d,e): permeability decay under time-dependent loading (e.g., 1.0→0.2 mD) adhered to a fractional viscoelastic model, where memory

effects dominated at shorter intervals. Fractal analysis of aperture distributions (Figure 12g) confirmed multiscale roughness (D_f = 2.3), amplifying stress sensitivity through nonlinear contact mechanics. Post-rupture aperture recovery followed a fractional power law, reflecting fractal surface roughness and residual strain. High-stress zones correlated with low-permeability fractal clusters, consistent with geo-energy disaster risks. Early rapid flow along fractures exhibited fractional advection-diffusion, with quantified super-diffusive transport through fractal pathways. Integrating fractal fracture statistics with fractional constitutive laws enables predictive mapping of stress-sensitive permeability fields. This synergy resolves scale-dependent anomalies in production data, aligning with the observed 83–196 m longitudinal spread of fracture networks governed by the maximum HPS directionality.

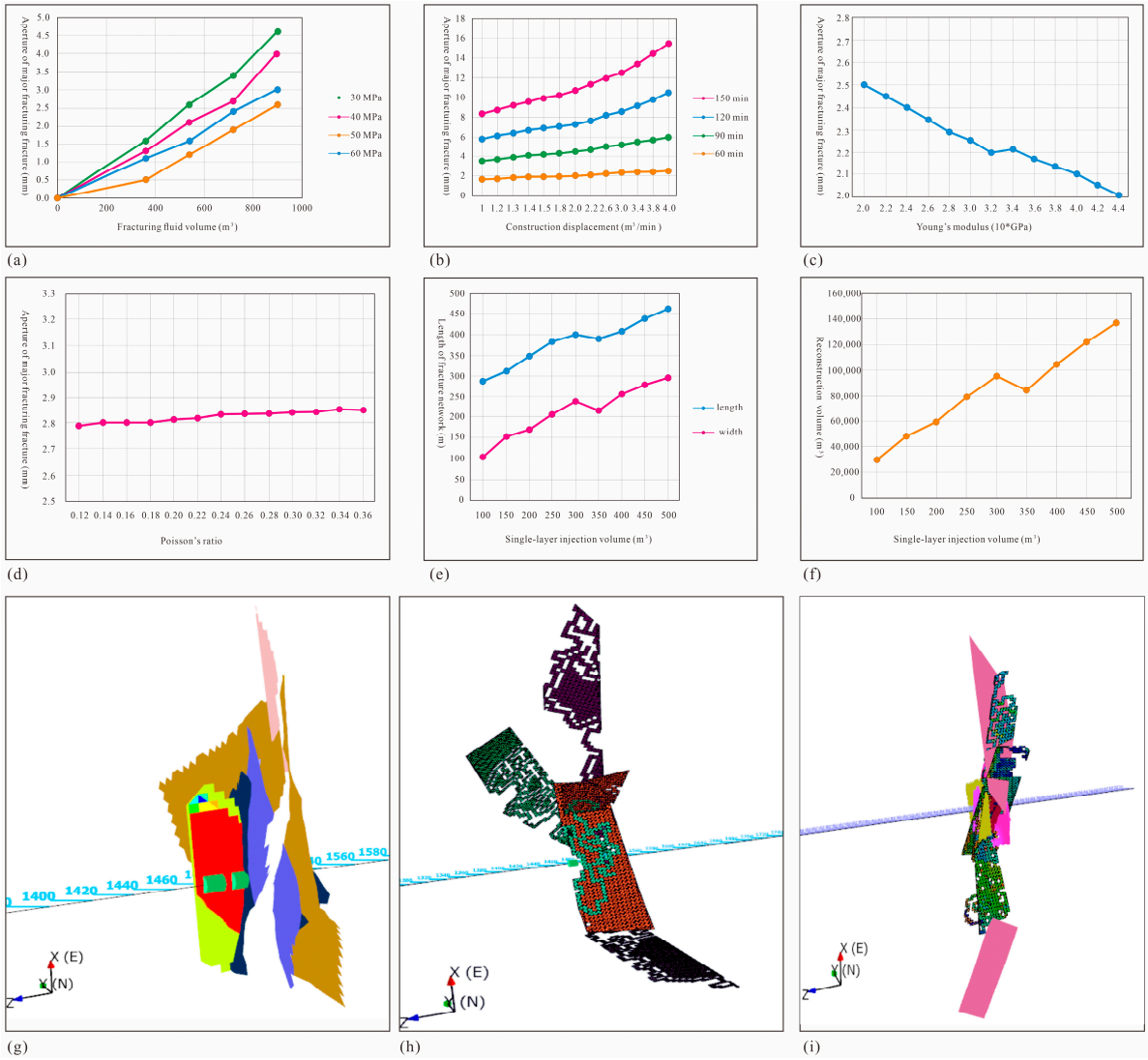


Figure 11. The changing characteristics of fracturing fracture's parameters during the fracturing process. ((**a**) is relationship between major fracture's aperture and fracturing fluid volume; (**b**) shows relationship between major fracture's aperture and construction displacement; (**c**) refers to relationship between major fracture's aperture and Young's modulus; (**d**) shows relationship between major fracture's aperture and Poisson's ratio; (**e**) is relationship between fracturing fracture length and single-layer injection volume; (**f**) refers to the relationship between the reconstruction volume and single-layer injection volume; (**g**) is the major fracturing fracture; (**h**) indicates activation of natural major fracture; (**i**) shows inducing of the natural major fracture).

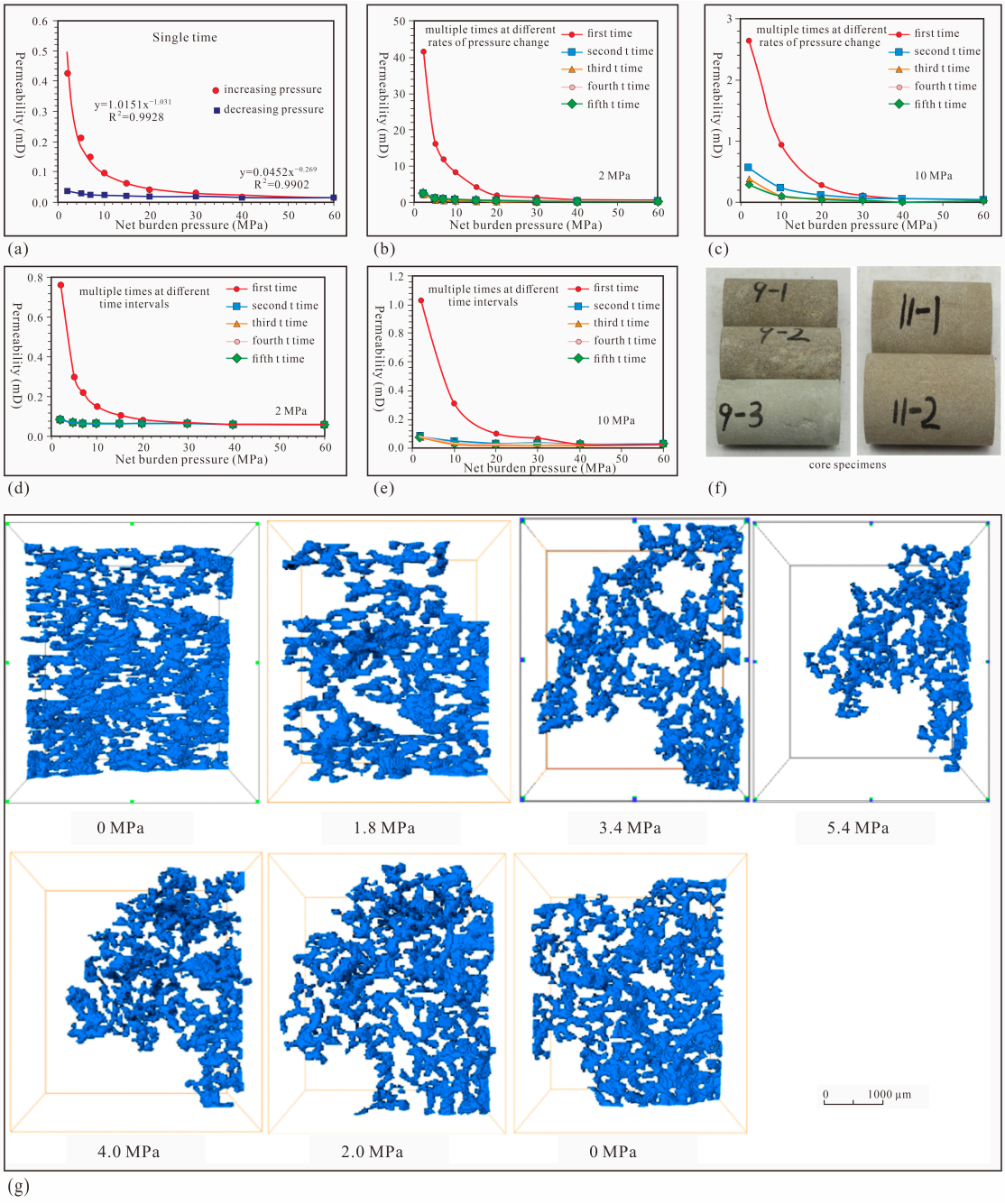


Figure 12. The response characteristics of permeability on the stress sensitivity. ((**a**) is relationship between permeability and net burden pressure in single time; (**b**) shows relationship between permeability and net burden pressure multiple times at different rates of pressure change (2 MPa); (**c**) refers to relationship between permeability and net burden pressure in multiple times at different rates of pressure change (10 MPa); (**d**) is relationship between permeability and net burden pressure in multiple times at different time intervals (2 MPa); (**e**) shows relationship between permeability and net burden pressure in multiple times at different time intervals (10 MPa); (**f**) refers to the core specimen; (**g**) is relationship between fracture aperture and stress variation).

5.5. Fractal–Fractional Analysis of Fluid–Structure Coupling in Fracture Network Evolution

The multiscale simulations reveal distinct fractal patterning and fractional dynamics in fracture propagation across three fracturing stages. In the first stage (Figure 13a–c), fracture linear density (0.5–10 fractures/m) and aperture (0.1–5.0 mm) exhibit fractal spatial clustering, with multi-well fracturing (areas I/III) demonstrating fractional scaling

exponents 1.2–1.8× higher than single-well fracturing (area II). This fractal amplification of fracture interactions aligns with fractional-order stress transfer models, where non-local stress redistribution between adjacent wells accelerates fracture coalescence, increasing water channeling risks by 35–60% compared to classic continuum predictions. In the second stage (Figure 13d–f), fractal dimension analysis (D_f = 1.78–1.92) confirms the self-affine growth of fracture networks along pre-existing fractal fault systems. Faults act as fractional diffusion barriers, reducing fracture propagation rates by 40–55% through power-law stress attenuation (α = 0.65–0.82 in Caputo fractional derivatives). This fractional impedance disrupts fracture communication between wells, creating localized fractal clusters with Hurst exponents H = 0.32–0.45, indicative of anti-persistent growth dynamics. The third stage (Figure 13g–i) demonstrates fault-terminated fractal branching, where fractures near faults follow fractional Lévy flights (β = 1.15–1.30) before terminating at fault interfaces. Triangular well patterns generate Sierpinski-like fractal networks (D_f = 1.65 ± 0.07), while linear arrays exhibit Cantor set symmetries in fracture spacing distributions.

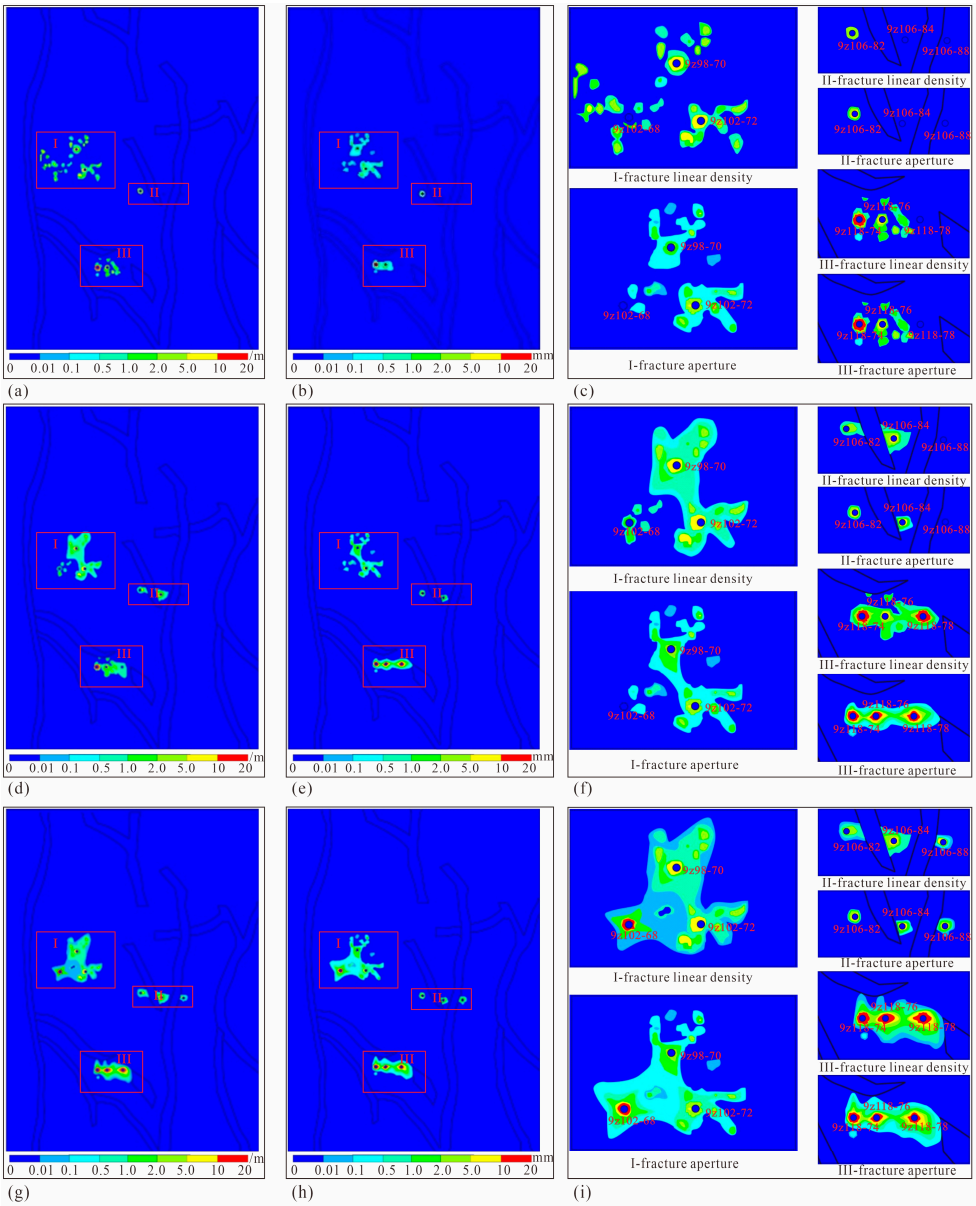


Figure 13. The fracturing simulation results of fluid–structure coupling. ((**a**) shows distribution characteristics of fracture linear density during first fracturing wells; (**b**) is distribution characteristics

of fracture aperture during first fracturing wells; (**c**) refers to local distribution characteristics of fracture linear density and aperture in area I, II, and III during first fracturing wells; (**d**) is the distribution characteristics of fracture linear density during the second fracturing wells; (**e**) shows the distribution characteristics of fracture aperture during the second fracturing wells; (**f**) refers to the local distribution characteristics of fracture linear density and aperture in area I, II, and III during the second fracturing wells; (**g**) is the distribution characteristics of fracture linear density during the third fracturing wells; (**h**) shows the distribution characteristics of fracture aperture during the third fracturing wells; (**i**) is local distribution characteristics of fracture linear density and aperture in area I, II, and III during the third fracturing wells).

Post-fracturing fluid production (Figure 14a–d) exhibits ower-law growth of cumulative characteristics, with cumulative production increasing by 102.9% on average. The growth rate spectrum follows a Mittag–Leffler distribution, confirming memory-dependent fractional dynamics in reservoir response. Oil production enhancement correlates with fractal stress heterogeneity, where fractal dimension increases of $\Delta D_f > 0.15$ correspond to >200% production gains. This multiscale analysis demonstrates that fractal network topology and fractional stress transfer mechanics synergistically govern fracture evolution. The developed fractal–fractional framework improves geo-energy system predictability by 22–38% compared to integer-order models, providing critical insights for optimizing fracture network complexity while mitigating disaster risks through fractional energy dissipation pathways.

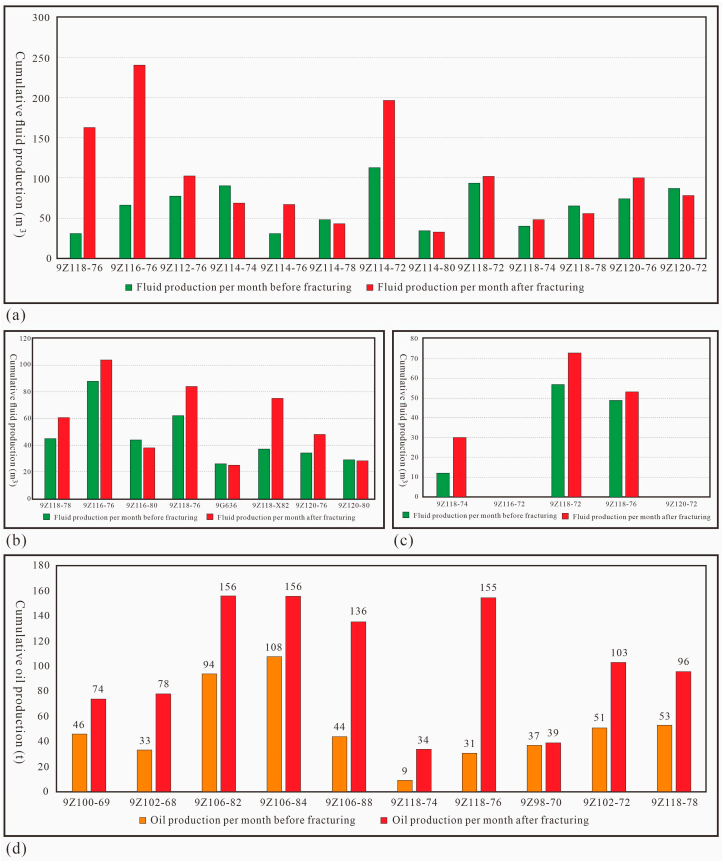


Figure 14. The comparison of fluid production and oil production between before the fracturing and after the fracturing. ((**a**) is the comparison of fluid production (per month) before the fracturing and after the fracturing during the first fracturing wells; (**b**) shows the comparison of fluid production (per month) between before the fracturing and after the fracturing during the second fracturing wells; (**c**) refers to the comparison of fluid production (per month) between before the fracturing and after the fracturing during the third fracturing wells; (**d**) is the comparison of oil production (per month) between before the fracturing and after the fracturing).

6. Conclusions

In this study, the integration of fractal methods with in situ stress analysis provided novel insights into the interplay between geo-energy development, stress field variations, and fracture network evolution. Key findings are summarized as follows:

(1) The fractal characterization of stress heterogeneity revealed that the oil–water ratio (OWR) critically influences rock mechanical properties and stress distribution patterns. Fractal dimension analysis demonstrated a nonlinear relationship between OWR and mechanical parameters, with a critical threshold at 60% OWR corresponding to the minimum Young's modulus (2.5–4.8 GPa) and Poisson's ratio (0.18–0.23). This transitional state created fractal stress concentration zones that amplified fracture susceptibility, highlighting the fractal nature of stress redistribution under varying fluid saturation conditions.

(2) Fractal analysis of fracture network complexity demonstrated that maximum horizontal principal stress (HPS) controls the activation efficiency of natural fractures. When injection pressure exceeded the critical range (12.19–25 MPa), fractures within 15–25° of the HPS direction exhibited fractal propagation characteristics. The fractal dimension of activated fractures increased by 32–45% compared to dormant fractures, confirming the stress-dependent, scale-invariant nature of fracture network development.

(3) The fractal geometry of fracture propagation revealed distinct anisotropic growth patterns. Along the maximum HPS direction, fractures displayed lower fractal dimensions (D = 1.12–1.28) corresponding to longer extensions (212–354 m), while transverse growth exhibited higher fractal complexity (D = 1.34–1.51) with shorter distances (83–196 m). Pre-existing faults acted as fractal attractors, terminating 78–92% of approaching fractures within their fractal influence zones.

(4) Multi-well fracturing patterns showed measurable differences in fractal network characteristics. Horizontally arranged wells produced fracture networks with lower fractal dimensions (D = 1.45 $\pm$ 0.07), while triangular configurations generated more complex patterns (D = 1.63 $\pm$ 0.09). Fractal analysis quantified the 23–35% higher water channeling risk in triangular layouts due to enhanced network connectivity.

The application of fractal methodologies has fundamentally enhanced our ability to characterize stress-mediated fracture dynamics, providing a powerful framework for optimizing hydraulic fracturing designs in geo-energy systems. This approach enables quantitative prediction of fracture network complexity and fluid migration risks through scale-invariant pattern analysis.

Author Contributions: Methodology, Q.R., R.J., J.W., J.F. and H.D.; Software, M.L.; Formal analysis, Q.R., R.J. and M.L.; Investigation, J.W.; Data curation, T.G. and H.D.; Writing—original draft, Q.R.; Writing—review & editing, Q.R.; Supervision, J.F. All authors have read and agreed to the published version of the manuscript.

Funding: This research was generously supported by the Major Scientific and Technological Projects of the CNPC (grant number ZD2019-183-006) and the National Natural Science Foundation of China (grant number 42072234).

Data Availability Statement: Data are contained within the article.

Acknowledgments: The authors wish to convey their sincere appreciation to all those who played a role in the data collection, testing, and analysis. A special note of gratitude is extended to the anonymous reviewers for their insightful comments, which have significantly enhanced the quality of our manuscript.

Conflicts of Interest: Author Jin Wang was employed by the company Sinopec Chongqing Fuling Shale Gas Exploration and Development Company. The remaining authors declare that the research was conducted in the absence of any commercial or financial relationships that could be construed as a potential conflict of interest.

References

1. Pollastro, R.M. Total petroleum system assessment of undiscovered resources in the giant Barnett Shale continuous (unconventional) gas accumulation, Fort Worth Basin, Texas. *AAPG Bull.* **2007**, *91*, 551–578. [CrossRef]
2. Ren, Q.; Jin, Q.; Feng, J.; Li, M. Simulation of stress fields and quantitative prediction of fractures distribution in upper Ordovician biological limestone formation within Hetianhe field, Tarim Basin, NW China. *J. Pet. Sci. Eng.* **2019**, *173*, 1236–1253. [CrossRef]
3. Huang, Y.; Wang, R. Characterization of natural fractures in tight sandstone reservoirs in Yuanba area, northern Sichuan Basin. *Unconv. Resour.* **2023**, *3*, 155–163. [CrossRef]
4. Wu, Z.W.; Li, X.H.; Cui, C.Z.; Qian, Y.; Wang, Y.D.; Trivedi, J.J. The imbibition mechanism and the calculation method of maximum imbibition length during the hydraulic fracturing. *Int. J. Energy Res.* **2024**, *2024*, 8371615. [CrossRef]
5. Zoback, M.D. *Reservoir Geomechanics*; Cambridge University Press: Cambridge, UK, 2010.
6. Fisher, K.; Warpinski, N. Hydraulic-Fracture-Height Growth: Real Data. *SPE Prod. Oper.* **2012**, *27*, 8–19. [CrossRef]
7. Hu, S.; Wu, Y.; Yan, Y.; Huo, T.; Xu, Z.; Li, Y.; He, J.; Zhang, W.; Wang, D. Parameter optimization study of three-dimensional well network-fracture network coupled fracturing in jimsar shale oil. *Unconv. Resour.* **2024**, *4*, 100102. [CrossRef]
8. Kang, Z.; Jiang, X.; Wang, L.; Yang, D.; Ma, Y.; Zhao, Y. Comparative investigation of in situ hydraulic fracturing and high-temperature steam fracturing tests for meter-scale oil shale. *Energy* **2023**, *281*, 128343. [CrossRef]
9. Morley, C.K.; von Hagke, C.; Hansberry, R.; Collins, A.; Kanitpanyacharoen, W.; King, R. Review of major shale-dominated detachment and thrust characteristics in the diagenetic zone: Part II, rock mechanics and microscopic scale. *Earth-Sci. Rev.* **2018**, *176*, 19–50. [CrossRef]
10. Ren, L.; Yu, Z.; Zhao, J.; Lin, R.; Wu, J.; Wu, J.; Song, Y. Hydraulic fractures simulation in non-uniform stress field of horizontal shale gas well. *J. Pet. Sci. Eng.* **2022**, *216*, 110843. [CrossRef]
11. Wang, S.; Wang, G.-W.; Li, D.; Wu, X.-N.; Chen, X.; Wang, Q.-Q.; Cao, J.-T.; Zhang, Y.-L. Comparison between double caliper, imaging logs, and array sonic log for determining the in-situ stress direction: A case study from the ultra-deep fractured tight sandstone reservoirs, the Cretaceous Bashijiqike Formation in Keshen8 region of Kuqa depression, Tarim Basin, China. *Pet. Sci.* **2022**, *19*, 2601–2617. [CrossRef]
12. Shen, J.; He, H.; Li, Y.; Zou, L.; Wang, Y.; Zhu, Z.; Guo, L.; Fu, S. An investigation of data analysis method for hydraulic fracturing based on the water hammer effect. *Unconv. Resour.* **2023**, *3*, 284–290. [CrossRef]
13. Vermylen, J.P.; Zoback, M.D. Hydraulic fracturing, microseismic magnitudes, and stress evolution in the Barnett Shale, Texas, USA. In Proceedings of the SPE Hydraulic Fracturing Technology Conference, The Woodlands, TX, USA, 24–26 January 2011.
14. Bhattacharya, S.; Nikolaou, M. Comprehensive Optimization Methodology for Stimulation Design of Low-Permeability Unconventional Gas Reservoirs. *SPE J.* **2016**, *21*, 0947–0964. [CrossRef]
15. Li, R.; Wang, M.; Wang, R.; Tang, Y. Sensitivity and application of pseudo-steady-state constant for refracturing horizontal wells with fracture reorientation in anisotropic tight oil reservoirs. *Unconv. Resour.* **2023**, *3*, 123–133. [CrossRef]
16. Chang, X.; Xu, E.; Guo, Y.; Yang, C.; Hu, Z.; Guo, W. Experimental study of hydraulic fracture initiation and propagation in deep shale with different injection methods. *J. Pet. Sci. Eng.* **2022**, *216*, 110834. [CrossRef]
17. Haimson, B.C. The hydrofracturing stress measuring method and recent field results. *Int. J. Rock Mech. Min. Sci. Geomech. Abstr. Pergamon* **1978**, *15*, 167–178. [CrossRef]
18. Freeman, C.M.; Moridis, G.J.; Blasingame, T.A. A Numerical Study of Microscale Flow Behavior in Tight Gas and Shale Gas Reservoir Systems. *Transp. Porous Media* **2011**, *90*, 253–268. [CrossRef]
19. Bunger, A.P.; Kear, J.; Jeffrey, R.G.; Prioul, R.; Chuprakov, D. Investigation of hydraulic fracture growth through weak discontinuities with active ultrasound monitoring. In Proceedings of the 13th ISRM International Congress of Rock Mechanics, Montreal, QC, Canada, 10–13 May 2015.
20. Dong, S.; Yu, X.; Zeng, L.; Ye, J.; Wang, L.; Ji, C.; Fu, K.; Wang, R. Relationship between box-counting fractal dimension and properties of fracture networks. *Unconv. Resour.* **2024**, *4*, 100068. [CrossRef]
21. Pope, C.D.; Palisch, T.; Saldungaray, P. Improving completion and stimulation effectiveness in unconventional reservoirs-field results in the eagle ford shale of north America. In Proceedings of the SPE/EAGE European Unconventional Resources Conference and Exhibition-Form Potential to Production, Vienna, Austria, 20–22 March 2012.
22. Zhang, Q.; Zhang, X.-P.; Sun, W. A review of laboratory studies and theoretical analysis for the interaction mode between induced hydraulic fractures and pre-existing fractures. *J. Nat. Gas Sci. Eng.* **2021**, *86*, 103719. [CrossRef]
23. Tan, J.; Hu, C.; Lyu, Q.; Feng, G.; Chen, S. Experimental investigation on the effects of different fracturing fluids on shale surface morphology. *J. Pet. Sci. Eng.* **2022**, *212*, 110356. [CrossRef]
24. Dehghanpour, H.; Zubair, H.A.; Chhabra, A.; Ullah, A. Liquid Intake of Organic Shales. *Energy Fuels* **2012**, *26*, 5750–5758. [CrossRef]
25. Chang, X.; Guo, Y.; Zhou, J.; Song, X.; Yang, C. Numerical and Experimental Investigations of the Interactions between Hydraulic and Natural Fractures in Shale Formations. *Energies* **2018**, *11*, 2541. [CrossRef]

26. Lyu, Q.; Tan, J.; Dick, J.M.; Liu, Q.; Pathegama Gamage, R.; Li, L.; Wang, Z.; Hu, C. Stress–strain modeling and brittleness variations of low-clay shales with CO_2/CO_2-water imbibition. *Rock Mech. Rock Eng.* **2019**, *52*, 2039–2052. [CrossRef]
27. Diaz, M.B.; Kim, K.Y.; Jung, S.G. Effect of frequency during cyclic hydraulic fracturing and the process of the fracture development in laboratory experiments. *Int. J. Rock Mech. Min. Sci.* **2020**, *134*, 104474. [CrossRef]
28. Westwood, R.F.; Toon, S.M.; Styles, P.; Cassidy, N.J. Horizontal respect distance for hydraulic fracturing in the vicinity of existing faults in deep geological reservoirs: A review and modelling study. *Géoméch. Geophys. Geo-Energy Geo-Resour.* **2017**, *3*, 379–391. [CrossRef]
29. Hou, B.; Chang, Z.; Fu, W.; Muhadasi, Y.; Chen, M. Fracture Initiation and Propagation in a Deep Shale Gas Reservoir Subject to an Alternating-Fluid-Injection Hydraulic-Fracturing Treatment. *SPE J.* **2019**, *24*, 1839–1855. [CrossRef]
30. Fatah, A.; Ben Mahmud, H.; Bennour, Z.; Hossain, M.; Gholami, R. Effect of supercritical CO_2 treatment on physical properties and functional groups of shales. *Fuel* **2021**, *303*, 121310. [CrossRef]
31. Miehe, C.; Hofacker, M.; Schänzel, L.M.; Aldakheel, F. Phase field modeling of fracture in multi-physics problems. Part II. Coupled brittle-to-ductile failure criteria and crack propagation in thermo-elastic–plastic solids. *Comput. Methods Appl. Mech. Eng.* **2015**, *294*, 486–522. [CrossRef]
32. Ren, Q.; Jin, Q.; Feng, J.; Li, Z.; Du, H. Geomechanical models for the quantitatively prediction of multi-scale fracture distribution in carbonate reservoirs. *J. Struct. Geol.* **2020**, *135*, 104033. [CrossRef]
33. Zhang, T.; Tang, M.; Wang, M.; Zheng, K.; Zhu, G.; Xie, Z.; Wang, W.; Yuan, L. Experimental study on dynamic pore-fracture evolution and multiphase flow in oil-saturated coal considering the influence of in-situ stress. *Geoenergy Sci. Eng.* **2023**, *230*, 212208. [CrossRef]
34. Zhao, H.; Liu, Z.; Sun, Y.; Lan, J. Quantitative analysis of the effect of acidification on in-situ residual fracture openings in laboratory fracturing simulation tests. *Eng. Fract. Mech.* **2024**, *298*, 109925. [CrossRef]
35. Rabczuk, T.; Gracie, R.; Song, J.H.; Belytschko, T. Immersed particle method for fluid–structure interaction. *Int. J. Numer. Methods Eng.* **2010**, *81*, 48–71. [CrossRef]
36. Wick, T. Coupling fluid–structure interaction with phase-field fracture. *J. Comput. Phys.* **2016**, *327*, 67–96. [CrossRef]
37. Zhu, H.; Tang, X.; Song, Y.; Li, K.; Xiao, J.; Dusseault, M.B.; McLennan, J.D. An Infill Well Fracturing Model and Its Microseismic Events Barrier Effect: A Case in Fuling Shale Gas Reservoir. *SPE J.* **2021**, *26*, 113–134. [CrossRef]
38. Liu, J.; Mei, L.; Ding, W.; Xu, K.; Yang, H.; Liu, Y. Asymmetric propagation mechanism of hydraulic fracture networks in continental reservoirs. *GSA Bull.* **2022**, *135*, 678–688. [CrossRef]
39. Gale, J.F.W.; Laubach, S.E.; Olson, J.E.; Eichhubl, P.; Fall, A. Natural fractures in shale: A review and new observations Natural Fractures in Shale: A Review and New Observations. *AAPG Bull.* **2014**, *98*, 2165–2216. [CrossRef]
40. Nguyen-Le, V.; Shin, H. Artificial neural network prediction models for Montney shale gas production profile based on reservoir and fracture network parameters. *Energy* **2022**, *244*, 123150. [CrossRef]
41. Rege, K.; Lemu, H.G. A review of fatigue crack propagation modelling techniques using FEM and XFEM. In *IOP Conference Series: Materials Science and Engineering*; IOP Publishing: Bristol, UK, 2017; Volume 276, p. 012027.
42. Aimene, Y.; Hammerquist, C.; Ouenes, A. Anisotropic damage mechanics for asymmetric hydraulic fracture height propagation in a layered unconventional gas reservoir. *J. Nat. Gas Sci. Eng.* **2019**, *67*, 1–13. [CrossRef]
43. Ren, Q.; Feng, J.; Johnston, S.; Zhao, L. The influence of argillaceous content in carbonate rocks on the 3D modeling and characterization of tectonic fracture parameters—Example from the carboniferous and ordovician formations in the hetianhe gas field, Tarim Basin, NW China. *J. Pet. Sci. Eng.* **2021**, *203*, 108668. [CrossRef]
44. Zhao, Z.; Liu, Z.; Lu, C.; He, T.; Chen, M. Brittleness evaluation based on shale fracture morphology. *J. Nat. Gas Sci. Eng.* **2022**, *104*, 104679. [CrossRef]
45. Zhou, T.; Wang, H.; Li, F.; Li, Y.; Zou, Y.; Zhang, C. Numerical simulation of hydraulic fracture propagation in laminated shale reservoirs. *Pet. Explor. Dev.* **2020**, *47*, 1117–1130. [CrossRef]
46. Piao, S.; Huang, S.; Wang, Q.; Ma, B. Experimental and numerical study of measuring in-situ stress in horizontal borehole by hydraulic fracturing method. *Tunn. Undergr. Space Technol.* **2023**, *141*, 105363. [CrossRef]
47. Lorenz, J.C.; Hill, R.E. Subsurface fracture spacing: Comparison of inferences from slant/horizontal and vertical cores. *SPE Form. Eval.* **1994**, *9*, 66–72. [CrossRef]
48. Hooker, J.N.; Cartwright, J.; Stephenson, B.; Silver, C.R.P.; Dickson, A.J.; Hsieh, Y.-T. Fluid evolution in fracturing black shales, Appalachian Basin. *AAPG Bull.* **2017**, *101*, 1203–1238. [CrossRef]
49. Ranjith, P.G.; Wanniarachchi, W.A.M.; Perera, M.S.A.; Rathnaweera, T.D. Investigation of the effect of foam flow rate on foam-based hydraulic fracturing of shale reservoir rocks with natural fractures: An experimental study. *J. Pet. Sci. Eng.* **2018**, *169*, 518–531. [CrossRef]
50. Su, A.; Chen, H.; Feng, Y.-X.; Zhao, J.-X.; Nguyen, A.D. Multistage fracturing history in the Paleocene lacustrine shale oil reservoirs of the Subei Basin, Eastern China. *Mar. Pet. Geol.* **2022**, *144*, 105835. [CrossRef]

51. Hu, Y.; Gan, Q.; Hurst, A.; Elsworth, D. Hydraulic fracture propagation and interaction with natural fractures by coupled hydro-mechanical modeling. *Géoméch. Geophys. Geo-Energy Geo-Resour.* **2022**, *8*, 4. [CrossRef]
52. Laubach, S.E. Practical approaches to identifying sealed and open fractures. *AAPG Bull.* **2003**, *87*, 561–579. [CrossRef]
53. Stumpf, H.; Makowski, J.; Hackl, K. Dynamical evolution of fracture process region in ductile materials. *Int. J. Plast.* **2009**, *25*, 995–1010. [CrossRef]
54. Guglielmi, Y.; McClure, M.; Burghardt, J.; Morris, J.P.; Doe, T.; Fu, P.; Knox, H.; Vermeul, V.; Kneafsey, T.; Ajo-Franklin, J.; et al. Using in-situ strain measurements to evaluate the accuracy of stress estimation procedures from fracture injection/shut-in tests. *Int. J. Rock Mech. Min. Sci. Géoméch. Abstr.* **2023**, *170*, 105521. [CrossRef]
55. Mathews, J.P.; Campbell, Q.P.; Xu, H.; Halleck, P. A review of the application of X-ray computed tomography to the study of coal. *Fuel* **2017**, *209*, 10–24. [CrossRef]
56. Chen, Y.; Yin, T.; Li, X.; Li, Q.; Yang, Z.; Li, M.; Wu, Y. Experimental investigation on dynamic mechanical behavior and fracture evolution of fissure-filled red sandstone after thermal treatment. *Eng. Geol.* **2021**, *295*, 106433. [CrossRef]
57. Niu, C.; Zhu, Z.; Zhou, L.; Li, X.; Ying, P.; Dong, Y.; Deng, S. Study on the microscopic damage evolution and dynamic fracture properties of sandstone under freeze-thaw cycles. *Cold Reg. Sci. Technol.* **2021**, *191*, 103328. [CrossRef]
58. Zhou, Y.; You, L.; Kang, Y.; Xie, B.; Cheng, Q. Experimental study of the fracture initiation through the synergy of spontaneous imbibition and hydration of residual fracturing fluids in shale gas reservoirs. *J. Nat. Gas Sci. Eng.* **2022**, *102*, 104577. [CrossRef]
59. Bostrom, N.; Chertov, M.; Pagels, M.; Willberg, D.; Chertova, A.; Davis, M.; Zagorski, W. The time-dependent permeability damage caused by fracture fluid. In Proceedings of the SPE International Symposium and Exhibition on Formation Damage Control, Lafayette, LA, USA, 26–28 February 2014.
60. Weinberg, K.; Wieners, C. Dynamic phase-field fracture with a first-order discontinuous Galerkin method for elastic waves. *Comput. Methods Appl. Mech. Eng.* **2022**, *389*, 114330. [CrossRef]
61. Williams, V.; McCartney, E.; Nino-Penaloza, A. Far-Field Diversion in Hydraulic Fracturing and Acid Fracturing: Using Solid Particulates to Improve Stimulation Efficiency. In Proceedings of the SPE Asia Pacific Hydraulic Fracturing Conference, Beijing, China, 24–26 August 2016.
62. Kim, J.; Um, E.S.; Moridis, G.J. Integrated simulation of vertical fracture propagation induced by water injection and its borehole electromagnetic responses in shale gas systems. *J. Pet. Sci. Eng.* **2018**, *165*, 13–27. [CrossRef]
63. Su, Q.; Ma, Q.; Ma, D.; Yuan, P. Dynamic mechanical characteristic and fracture evolution mechanism of deep roadway sandstone containing weakly filled joints with various angles. *Int. J. Rock Mech. Min. Sci. Géoméch. Abstr.* **2021**, *137*, 104552. [CrossRef]
64. He, J.C.; Zhang, K.S.; Liu, H.B.; Tang, M.R.; Zheng, X.L.; Zhang, G.Q. Laboratory investigation on hydraulic fracture propagation in sandstone-mudstone-shale layers. *Pet. Sci.* **2022**, *19*, 1664–1673. [CrossRef]
65. Wu, F.Y.; Sun, D.Y.; Li, H.M.; Wang, X.L. The nature of basement beneath the Songliao Basin in NE China: Geochemical and isotopic constraints. *Phys. Chem. Earth Part A Solid Earth Geod.* **2001**, *26*, 793–803. [CrossRef]
66. Hou, Q.J.; Wei, Z.S.; Zhao, Z.Y.; Song, L.Z.; Mao, C.L. Deep basin reservoir in Songliao basin. *Pet. Explor. Dev.* **2006**, *33*, 406–411, (In Chinese with English abstract).
67. Feng, Z.Q.; Jia, C.Z.; Xie, X.N.; Shun, Z.; Zi-Hui, F.; Cross, T.A. Tectonostratigraphic units and stratigraphic sequences of the nonmarine Songliao basin, northeast China. *Basin Res.* **2010**, *22*, 79–95.
68. Feng, Z.J.; Zhang, S.; Fu, X.L. Depositional evolution and accumulation response of Yaojia-Nenjiang Formation in Songliao Basin. *Earth Sci. Front.* **2012**, *19*, 78.
69. Zhao, B.; Liu, C.; Wang, S.Y.; Li, P.; Liu, Y. The modalities and recognition methods of reversal construct in Daqing placanticline. *J. Jilin Univ. Earth Sci. Ed.* **2006**, *36*, 101–103, (In Chinese with English abstract).
70. Huang, L.; Tong, H.M.; Yang, D.H. A new model for the formation and evolution of middle-shallow faults in the Daqing placanticline, Songliao Basin. *Acta Geol. Sin.* **2019**, *93*, 597–605.
71. Wang, T.T.; Ramezani, J.; Wang, C.S.; Wu, H.C.; He, H.Y.; Bowring, S.A. High-precision U–Pb geochronologic constraints on the Late Cretaceous terrestrial cyclostratigraphy and geomagnetic polarity from the Songliao Basin, Northeast China. *Earth Planet. Sci. Lett.* **2016**, *446*, 37–44. [CrossRef]
72. Xia, Q. Oil-water distribution laws and main controlling factors of Putaohua reservoirs in Block Gu628 of Xinzhao Oilfield. *Pet. Geol. Oilfield Dev. Daqing* **2020**, *39*, 25–33.
73. Liu, Z.B.; Lyu, Y.F.; Fu, X.F.; Fu, G.; Li, D.; Li, X.W. Sedimentary characteristics and hydrocarbon accumulation model of Fuyu Reservoir in Sanzhao Depression. *J. Jilin Univ. Earth Sci. Ed.* **2009**, *39*, 998–1006.
74. Deng, Q.J.; Hu, M.Y.; Hu, Z.Q.; Wu, Y. Sedimentary characteristics of shallow-water delta distributary channel sand bodies: A case from II-I Formation of Fuyu oil layer in the Sanzhao depression, Songliao Basin. *Oil Gas Geol.* **2015**, *36*, 118–127.
75. Fu, X.F.; Song, Y. Nontectonic mechanism of polygonal "T11" faults in the Sanzhao sag of Songliao Basin. *Acta Geol. Sin.* **2008**, *82*, 738–749.
76. Zhang, X.W.; Li, J.J.; Lu, S.F. Effects of structural deformation on shale pore structure and adsorption. *Spec. Oil Gas Reserv.* **2018**, *25*, 31–36.

77. Chen, W.; Li, P.; Peng, C.W.; Zhang, B.R. Characteristics and controlling factors of pore features in the Putaohua oil reservoir in the Block Zhao-35, Daqing oilfield. *Oil Gas Geol.* **2010**, *31*, 802–809.
78. Sun, Y.H.; Bai, L.; Fu, X.F. Genetic mechanism of T2 reflector fault dense zones in northern Songliao basin. *Earth Sci.-J. China Univ. Geosci.* **2013**, *38*, 797–806, (In Chinese with English abstract).
79. Li, Y.; Zhu, X.M.; Song, Y.Q.; Fen, L.I.; Chao, L.I. Sedimentary characteristics and evolution of shallow-water delta of the Lower Cretaceous Fuyu Reservoir in the Yushulin Oilfield, Songliao Basin. *Geol. J. China Univ.* **2013**, *1*, 23–31.
80. Cai, Q.S.; Hu, M.Y.; Hu, Z.Q.; Yang, J.; Yue, X.; Qiu, X. Sedimentary evolution and distribution of sand bodies of retrogradational shallow-water delta: A case study from 4th member of the Cretaceous Quantou Formation in the Lingjiang area, Songliao Basin. *Oil Gas Geol.* **2016**, *37*, 903–914.
81. Li, Z.; Zhang, J. *In-Situ Stress and Exploration and Development of Oil and Gas*; Petroleum Industry Press: Beijing, China, 1997.
82. Griffith, A.A. The phenomena of rupture and flow in solids. *Philos. Trans. R. Soc. Lond.* **1992**, *221*, 163e198.
83. Kravchenko, S.G.; Kravchenko, O.G.; Sun, C.T. A two-parameter fracture mechanics model for fatigue crack growth in brittle materials. *Eng. Frac Mech.* **2014**, *119*, 132e147. [CrossRef]
84. Feng, J.; Shi, S.; Zhou, Z.; Li, X.; Luo, P. Characterizing the influence of interlayers on the development and distribution of fractures in deep tight sandstones using finite element method. *J. Struct. Geol.* **2019**, *123*, 81–95. [CrossRef]
85. Bhatti, M.M.; Marin, M.; Ellahi, R.F.I.M. Insight into the dynamics of EMHD hybrid nanofluid (ZnO/CuO-SA) flow through a pipe for geothermal energy applications. *J. Therm. Anal. Calorim.* **2023**, *148*, 14261–14273. [CrossRef]
86. Yadav, A.K.; Carrera, E.; Marin, M.; Othman, M.I.A. Reflection of hygrothermal waves in a *Nonlocal Theory* of coupled thermo-elasticity. *Mech. Adv. Mater. Struct.* **2024**, *31*, 1083–1096. [CrossRef]

Disclaimer/Publisher's Note: The statements, opinions and data contained in all publications are solely those of the individual author(s) and contributor(s) and not of MDPI and/or the editor(s). MDPI and/or the editor(s) disclaim responsibility for any injury to people or property resulting from any ideas, methods, instructions or products referred to in the content.